geosciences

MDPI

Article

Relations between Fault and Fracture Network Affecting the Lastoni di Formin Carbonate Platform (Italian Dolomites) and Its Deformation History

Niccolò Menegoni [1,*], Riccardo Inama [2], Yuri Panara [3], Matteo Crozi [1] and Cesare Perotti [1]

[1] Dipartimento di Scienze della Terra e dell'Ambiente, Università di Pavia, Via Adolfo Ferrata 4, 27100 Pavia, Italy
[2] Signal S.r.l., Via Fratelli Cuzio 42, 27100 Pavia, Italy
[3] Ali I. Al-Naimi Petroleum Engineering Research Center, King Abdullah University of Science and Technology, Thuwal 23955-6900, Saudi Arabia
* Correspondence: niccolo.menegoni@unipv.it; Tel.: +39-0382985846

Abstract: In this study, we analyze the fault and fracture network of the Middle Triassic carbonate platform of the Lastoni di Formin (Italian Dolomites, Italy). The reconstruction of the deformation history is of primary importance for a full comprehension of the present structural setting of this carbonate platform. The huge dimensions of the carbonate body and superb exposure of its vertical cliffs and gently dipping top plateau make the Lastoni di Formin platform an ideal outcrop to integrate traditional fieldwork with Digital Outcrop Modelling analysis. The results of the structural studies partially confirm that the present-day fracture pattern is the result of differential compaction-induced deformation that generated WNW-ESE-trending extensional fractures and normal faults, perpendicular to the direction of progradation of the platform. Successively, extensional tectonics, likely related to the Jurassic rifting phase, led to the formation of NNW-SSE striking fractures and westward-dipping normal faults. A Neogene compressional tectonic event, characterized by N-S to NW-SE crustal shortening, deformed the platform, essentially with strike-slip structures.

Keywords: outcrop analogues; structural analysis; faults; fractures; UAV; photogrammetry; DOM; VOM; dolomites; carbonate platform

Citation: Menegoni, N.; Inama, R.; Panara, Y.; Crozi, M.; Perotti, C. Relations between Fault and Fracture Network Affecting the Lastoni di Formin Carbonate Platform (Italian Dolomites) and Its Deformation History. *Geosciences* **2022**, *12*, 451. https://doi.org/10.3390/geosciences12120451

Academic Editors: Olivier Lacombe and Jesus Martinez-Frias

Received: 29 August 2022
Accepted: 5 December 2022
Published: 8 December 2022

1. Introduction

The Lastoni di Formin mountain relief consists of a dolomitized carbonate complex located in the central-eastern Dolomites (Italy) that, despite the relatively mild tectonic deformation that preserved most of the original depositional geometries, registered several subsequent tectonic events, which formed an extensive network of faults and fractures. In the Cassian carbonate platform exposed at the Lastoni di Formin and Nuvolau outcrops, the presence of early fractures has already been documented by previous studies [1,2], which show that they can be related to differential compaction of the underlying basinal facies [1,2], a widespread condition in Mesozoic carbonate platforms [3–10]. The clear recognition, identification, and definition of these early structures all around the carbonate bodies are often hampered by the complexity of faults and fracture networks. As suggested by [1,2], this may be due to different tectonic events that successively generated different sets of fractures with similar orientations or reactivated inherited ones. For this reason, and to better understand the tectonic history of the Lastoni di Formin, we performed a structural analysis of the different fault and fracture sets defining their relative timing and their correlation with the different deformation events that affected the study area.

We used a multiscale approach combining field investigation with proximal- and distal-remote sensing. The aerial (e.g., LiDAR and orthoimage) and Unmanned Aerial Vehicle (UAV)-based Digital Outcrop Model (DOM) data supported the collection of a

large dataset and enabled the acquisition of reliable georeferenced fracture parameters on remote and inaccessible parts of the outcrop, such as vertical cliffs (e.g., [11]), while field investigations provided a focus on the fracture features below the remote sensing resolution (e.g., <1 s–10 s of cm). The use of a multiscale approach is necessary because fractures occur at multiple scales, particularly at a sub-seismic resolution (<40 m) where the fracture density is extremely high [12]. This can be very important not only in structural studies but also in industrial applications, for example, in reservoir modeling, where heterogeneities of this dimension are often included in the matrix properties [13] and, therefore, multiscale studies are particularly important to cover the resolution gap between the core sample and the geophysical scale [14–17].

2. Geological and Structural Setting

The Lastoni di Formin massif is located in the eastern Dolomites (Italian Southern Alps) near Passo di Giau (46.477293° N, 12.083458° E—WGS84). The Dolomites are bounded to the north by the Insubric line and to the south by the south-verging Valsugana thrust [18] (Figure 1).

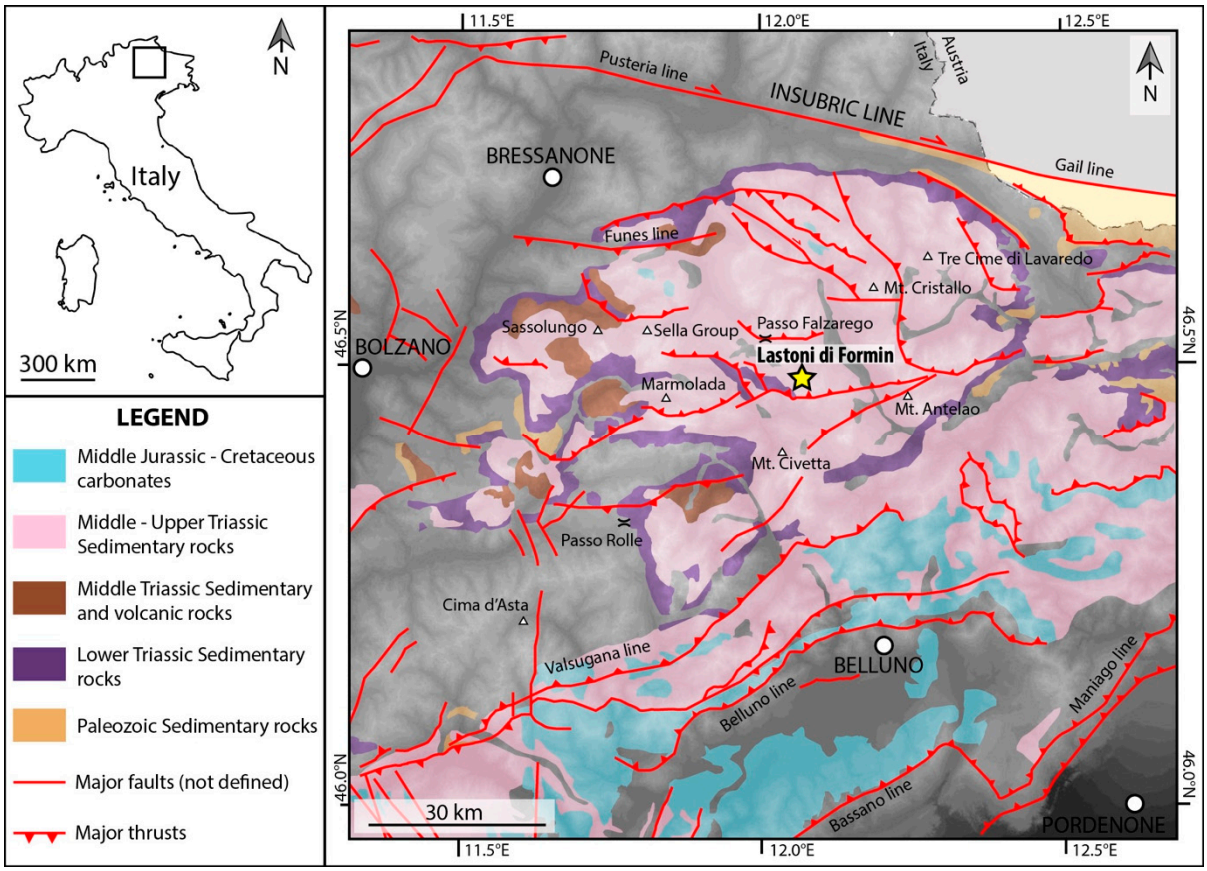

Figure 1. Simplified geological map of the central Dolomites region showing the major structural lineaments and the main sedimentary rocks from Paleozoic to Cretaceous (stratigraphy modified from [19,20]). The major structural lineaments were digitalized following the structural model at a scale of 1:500,000 from [21,22] and the geological map of Italy at a scale of 1:1,000,000 from [20] and integrating with the geological map at a scale of 1:50,000 from [23–27]. The background greyscale represents the Digital Elevation Model (DEM) of Italy (retrievable from [28]); lighter colors represent higher elevations.

The domain includes terrains only mildly deformed by tectonics from Permian to Jurassic; the landscape is dominated by spectacular Middle Triassic carbonate edifices. The relief of Lastoni di Formin represents the remnants of an exhumed carbonate platform

(so-called Cassian Dolomite) of Upper Ladinian–Lower Carnian age (Figure 2), and appears as a vast isolated plateau, gently tilted towards the north-east by approximately 15° and extending for over 2 km^2. It is bordered on the western and southern sides by vertical cliffs up to 250–300 m high. To the east, it is bounded by the Pinnacles of the Croda da Lago, carved into the Norian Dolomia Principale Formation.

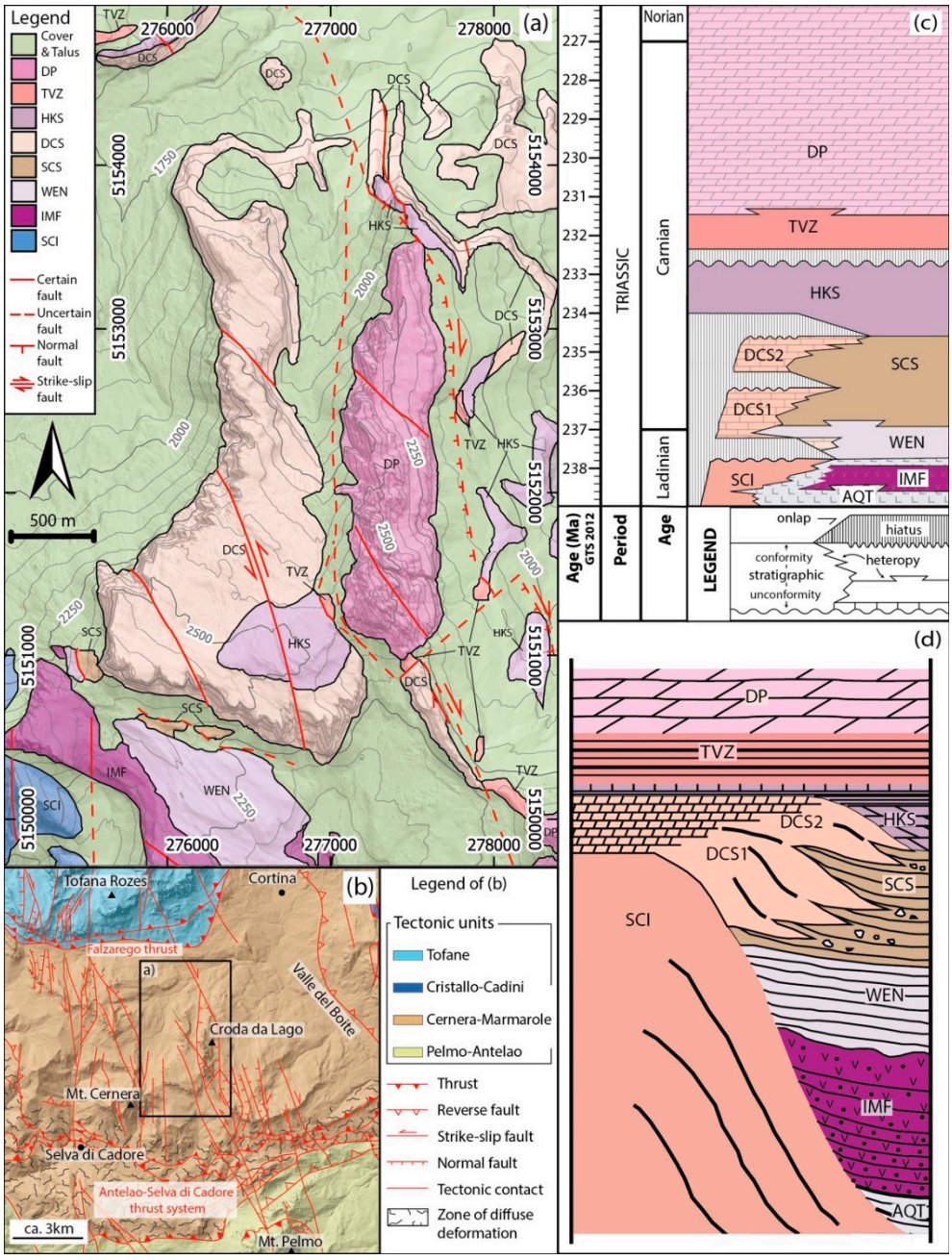

Figure 2. (**a**) Geological map of the study area (modified from [1]). (**b**) Simplified tectonic scheme of the study area and its surroundings (modified from [26]). (**c**) Stratigraphic framework of part of Middle and Upper Triassic of the central-eastern Dolomites (from [29], redrawn). (**d**) Simplified sketch of the stratigraphic relationships in the study area (modified after [1,26]). DP, Dolomia Principale; TVZ, Travenanzes Fm.; HKS, Heiligkreuz Fm.; DCS, Cassian Dolomite (differentiated in DSC1 and DSC2 according to [26]); SCS, San Cassiano Fm.; WEN, Wengen Fm.; SCI, Sciliar Fm.; IMF, Mt. Fernazza Fm.; AQT, Acquatona Fm.; LVN: Livinallongo Fm.

The Lastoni di Formin outcrop belongs to the Cernera-Marmarole (CM) tectonic unit (sensu [26,30]) (Figure 2b) that is delimited in the study area to the north by the Falzarego thrust and to the south by Antelao-Selva di Cadore thrust system. The Falzarego thrust, located to the west of Cortina, juxtaposes the Tofane unit with the CM unit [30]. To the south, the CM tectonic unit is overthrusted onto the Pelmo-Antelao unit through the south-verging Antelao-Selva di Cadore thrust system (Figure 2b). Moving from east to west, the complexity of the Antelao-Selva di Cadore thrust system increases [30], whereas in the eastern sector, it is constituted by a limited number of thrust planes, which juxtapose Dolomia Principale to Calcari Grigi Fm. (Lias). In the western sector, it involves more heterogeneous and ductile formations such as San Cassiano Fm. and Bellerophon Fm., forming a zone of diffuse deformation with a high geometric and kinematic complexity.

The Lastoni di Formin outcrop is formed by two superimposed carbonate complexes, separated by a horizontal unconformity [1]: The lower body is dominated by 10–15 m thick, low-angle, northward-dipping clinoforms, while the upper unit is organized in well-developed regular cycles of peritidal deposits that outcrop in the central and southern part of the massif and are connected to margin and slope facies (dipping 20°/25° to N/NE) in the northernmost sector. Individual cycles have a thickness ranging from 7–9 m to 1 m in the uppermost complex. However, the internal organization of the cycles and bed-parallel structures such as stylolites, enhanced by weathering (especially in the upper layers), create an apparent sub-metric stratification with a thickness of 20–50 cm. The lithology of the Cassian Dolomite consists of fine-grained greyish and whitish dolostone with a sucrose texture. The extensive dolomitization almost entirely obliterates the original depositional fabric and the sedimentary structures that are only locally visible. The Lastoni outcrop represents the easternmost part of a larger carbonate platform that includes, from west to east, the outcrops of Sass de Stria, Col Gallina, and Nuvolau-Averau [31–33].

The summit plateau is surmounted, in its southern sector, by the mixed carbonate-terrigenous deposits of the Heiligkreuz formation (sensu [26,34]). The onset of the Heiligkreuz formation marks the demise of the high-rimmed carbonate platforms, corresponding to a Tethys-scale crisis of the carbonate factories and a significant increase in the siliciclastic input [19,35,36]. According to several authors, this crisis was caused by a global episode of climate change, the "Carnian Pluvial Event" (CPE, [37,38]), which consists of a switch to humid conditions and increased rainfall and runoff at low latitudes, triggered by a major perturbation of the global carbon cycle [39–44]. The Heiligkreuz was deposited in a ramp environment that progressively filled the intraplatform basins, onlapping the platform slopes and leveling the paleotopography. In the study area, this formation corresponds to a ~50/60 m thick sequence consisting of a densely stratified carbonate basal unit (upper part of the Borca member), an intermediate unit comprising mainly marls and marly limestones with evident cross lamination (Dibona mb.), and a topmost unit represented by a 10–15 m thick massive oolitic bank, almost entirely dolomitized (Lagazuoi mb.) ([26]).

Tectonic Evolution of the Dolomites

During the Late Permian and Early Triassic, a rifting phase produced N-S-trending structural highs and lows [45]. The structural highs became the nucleus of shallow water carbonate production, which evolved and developed into carbonate buildups, while in the subsiding areas, the deposition of basinal units took place. During the Ladinian, sinistral transpressive tectonics occurred in the central Dolomites [18], developing flower structures and high-angle strike-slip faults concentrated along the alignment of the Stava fault and Cima Bocche anticline, characterized by an N70° strike. These structures are reported to cut the entire basement and sedimentary cover up to Early Ladinian rock [46]. Subsequently, these structures were crosscut by the Late Ladinian–Early Carnian intrusive complexes of Predazzo and Monzoni also associated with subaerial events (Sciliar, Monte Agnello) that occurred in the area [47,48].

From Late Triassic to Jurassic times, the Dolomites were subjected to rifting and progressively became part of the passive continental margin of the Adria plate [49,50],

associated with the opening of the western Alpine Tethys (Piedmont-Ligurian Ocean). This rifting led to the fragmentation of the large Dolomia Principale platform in structural highs and lows (Lombard Basin, the Trento Platform, the Belluno basin, and Friuli Platform) and was controlled by the presence of N-S striking normal faults. During the Paleogene and Neogene, the Southern Alpine domain was involved in the Alpine Orogeny, and the Dolomites became the innermost part of a south-vergent thrust belt [18,50]. The compressional tectonics started with the subduction of the Alpine Tethys Ocean during the Cretaceous phase [51,52], and extensive investigations have highlighted the presence of several distinct tectonic phases [53,54]. During the Dinaric phase (Chattian-Burdigalian), the maximum compressive axis was oriented to ENE-WSW [53–55]. Between Serravallian and Tortonian (Alpine—Valsuganense phase), N-S to NW-SE compression was recorded by the orientation of the major overthrusts (i.e., Valsugana and Belluno overthrusts, [18,53,55–57]. In the Late Messinian–Pliocene times, the last Alpine phase (Schledrense phase) was characterized by the reorientation of the σ1 axis to NW-SE [53,58], depicting an anticlockwise rotation of the main compressive direction from NE-SW to NW-SE [53,59].

3. Materials and Method

The massive dimensions of the Lastoni di Formin outcrop and the inaccessibility of its vertical cliffs represent a potential disadvantage for effective structural data collection using traditional fieldwork. Moreover, the field structural measurements are necessarily limited to a weighted number of sampling windows (mostly located on the topmost plateau) and suffer from truncation and occlusion related to the upper limit of the field 'resolution' (e.g., fracture traces cannot be correctly measured for their entire visible extension [60]) and the ineffective terrestrial point of view). As depicted by [1], the 3D nature of the Digital Outcrop Model (DOM) represents a valuable option to resolve these issues, allowing one to acquire quickly large volumes of three-dimensional, georeferenced digital measures at multiple scales, and distributed around the outcrop. For this reason, in this research, we used a multiscale approach combining field data with UAV-based DOM (proximal remote sensing) and aerial-based LiDAR and orthoimage (distal remote sensing) data covering a wide spectrum of measurement resolutions and sizes (Figure 3) that overlap each other.

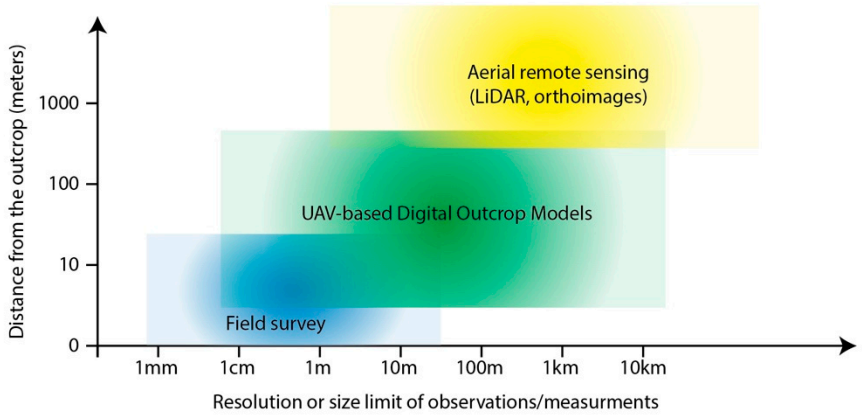

Figure 3. Schematic plots of the possible measurement resolutions achievable by the different techniques of investigation: The traditional field survey (direct-contact), UAV-based Digital Outcrop Models (proximal remote sensing), and aerial LiDAR and orthoimage (distal remote sensing).

3.1. Data

The UAV survey and the related development and accuracy assessment of the DOM of Lastoni di Formin (Figure 4) have been addressed in detail by [1] and are briefly described in Table 1.

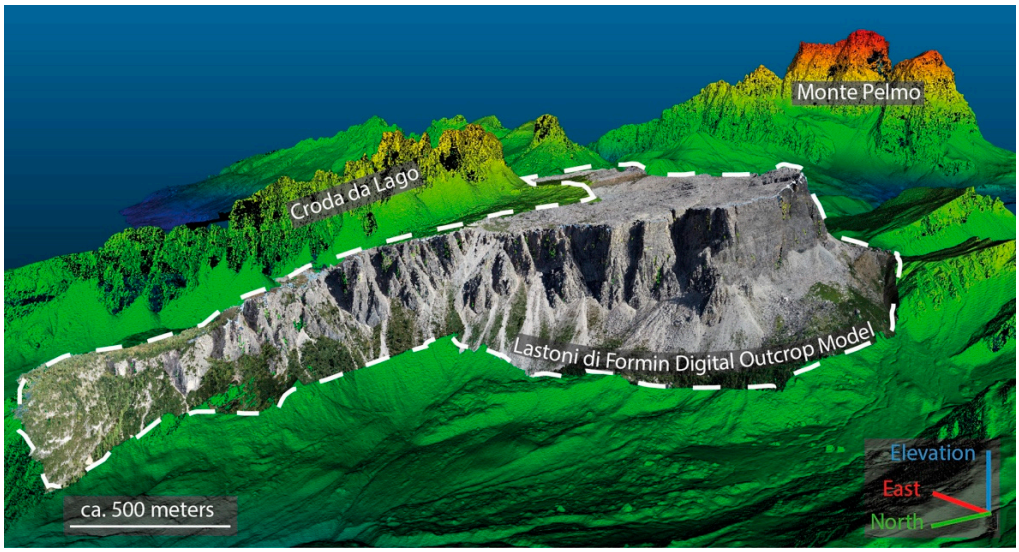

Figure 4. Perspective view of the Digital Outcrop Model (DOM) of the Lastoni di Formin, overlaying the 1 m resolution LiDAR (retrievable from [28]) colored according to the elevation (blue and red color correspond to lower and higher elevation, respectively).

Table 1. Summary of the main specifications of UAV instrumentation, the photogrammetric survey, and the developed Digital Outcrop Model (DOM) accuracy.

UAV type	Sensor type	Sensor resolution	Sensor size	Focal length
DJI Matrice 200	Zenmuse X4S (CMOS)	5472 × 3078 pixels	13.2 × 8.8 mm	8.8 mm
N. of flights	N. of photographs	Mean overlap and sidelap	Mean camera-outcrop distance	Mean resolution
16 (ca. 20 min each)	ca. 12,000	95%	200 m	5 cm/pixel
N. of Ground Control Points *	DOM mean horizontal absolute accuracy	DOM mean vertical absolute accuracy	DOM mean relative accuracy in length	DOM mean relative accuracy in orientation
22	120 cm	72 cm	0.17%	<1°

* Ground Control Points (GCPs) measured by a Topcon Hyper Pro RTK-GPS.

In this research, we used part of the dataset already presented by [1] composed of a field-based fracture dataset, a 3D line drawing of the bedding, and a 2D and 3D fault and fracture dataset, improved with high-detail new measurements.

The fracture dataset of [1] includes 523 2D fracture traces mapped onto the outcrop top plateau, stored as an SHP file and georeferenced in WGS84/UTM33N (EPSG:32,633), and 246 3D polylines and their 3D best-fit planes representing 246 fracture mapped onto the outcrop cliff, stored as georeferenced BIN files (CloudCompare format). During this research, the 2D dataset was improved by measuring 466 2D fault and fracture traces in order to perform a correct topological analysis of the fracture network. Therefore, the new improved 2D dataset is composed of a total amount of 989, obtaining fault and fracture traces. Similarly, the 3D dataset was improved with 218 new measurements to obtain a more representative picture of the 3D fault and fracture network. Therefore, the new and improved 3D fracture dataset is composed of 464 fault and fracture planes.

The 3D line drawing dataset of [1] is composed of 1059 3D polylines representing more than 150 bedding surfaces [1] stored as georeferenced BIN files (CloudCompare format). During this research, this dataset was improved by performing a global correlation of

the beds all along the rock cliffs, which allowed us to understand and measure the fault stratigraphic separation.

The field-based fracture dataset (449 measures) is compared with a new DOM-based high-resolution 2D fracture dataset composed of 3503 2D fracture traces. This new dataset will be further described.

3.2. Method

3.2.1. 2D Structural Analysis

The 2D structural analysis of the Lastoni di Formin was conducted in a GIS environment, by means of the open-source software QGIS [61] and using the LiDAR DEM (resolution 1 m) and AGEA2012 orthoimage (resolution 50 cm) [28]. Then, the fault and fracture trace dataset was improved, adding unmapped faults and fractures and repairing the trace topology. The repair of fracture topology was conducted using the Enable Snapping tool of QGIS and properly defining the fracture terminations/intersections. The acquisition of a topologically correct 2D fracture network allowed us to apply the NetworkGT algorithm, developed by [62], and perform the topological analysis of the 2D fracture network visible on the top of Lastoni di Formin outcrop.

The UAV-photogrammetric DEM and orthoimages were analyzed with a similar procedure on selected scan areas.

The digitized fault and fracture traces were then used to extract their attitude (trend) and length. As shown by [12], this approach could have some limitations, such as length truncation and censoring, which may be crucial only during fluid flow and permeability-related fracture network studies.

3.2.2. 3D Structural Analysis

The DOM was imported and sampled using CloudCompare stereo software [63] for the stereoscopic structural data interpretation and extraction, following the methodology presented in [11,60,64,65], and the faults, fractures, bedding altitudes and thickness, and stratigraphic separation were collected also using a semi-automatic picking tool embedded in the Compass plugin [66].

4. Results

The results of the fracture analysis (Figure 5) will be presented by describing (i) the fracture geometry (orientation and size), (ii) fracture displacement and kinematic, (iii) fracture intensity, and (iv) fracture network topology. The original dataset [1] was consistently improved with the recognition of several new fractures.

4.1. Fracture Orientation

The orientations of 989 2D faults and fracture traces (Figure 5a) can be grouped into three principal sets (Figure 6a): K1 with a mean trend of approximately 120° N, K2 with a mean trend of 154° N, and K3 with a mean trend of 21° N.

The 3D DOM analysis of the orientation of the fracture network was performed on 464 fracture planes affecting the rock cliffs. Four sets of faults and fractures (Figure 6b,c) can be distinguished: K1 with a mean attitude of 212°N/81° (dip direction and dip), which can be subdivided into K1a (200° N/86°) and K1b (216°N/79°); K2 with a mean attitude of 249°N/77°; K3 with a mean attitude of 287° N/86°; and K4 with a mean attitude of 165° N/77°.

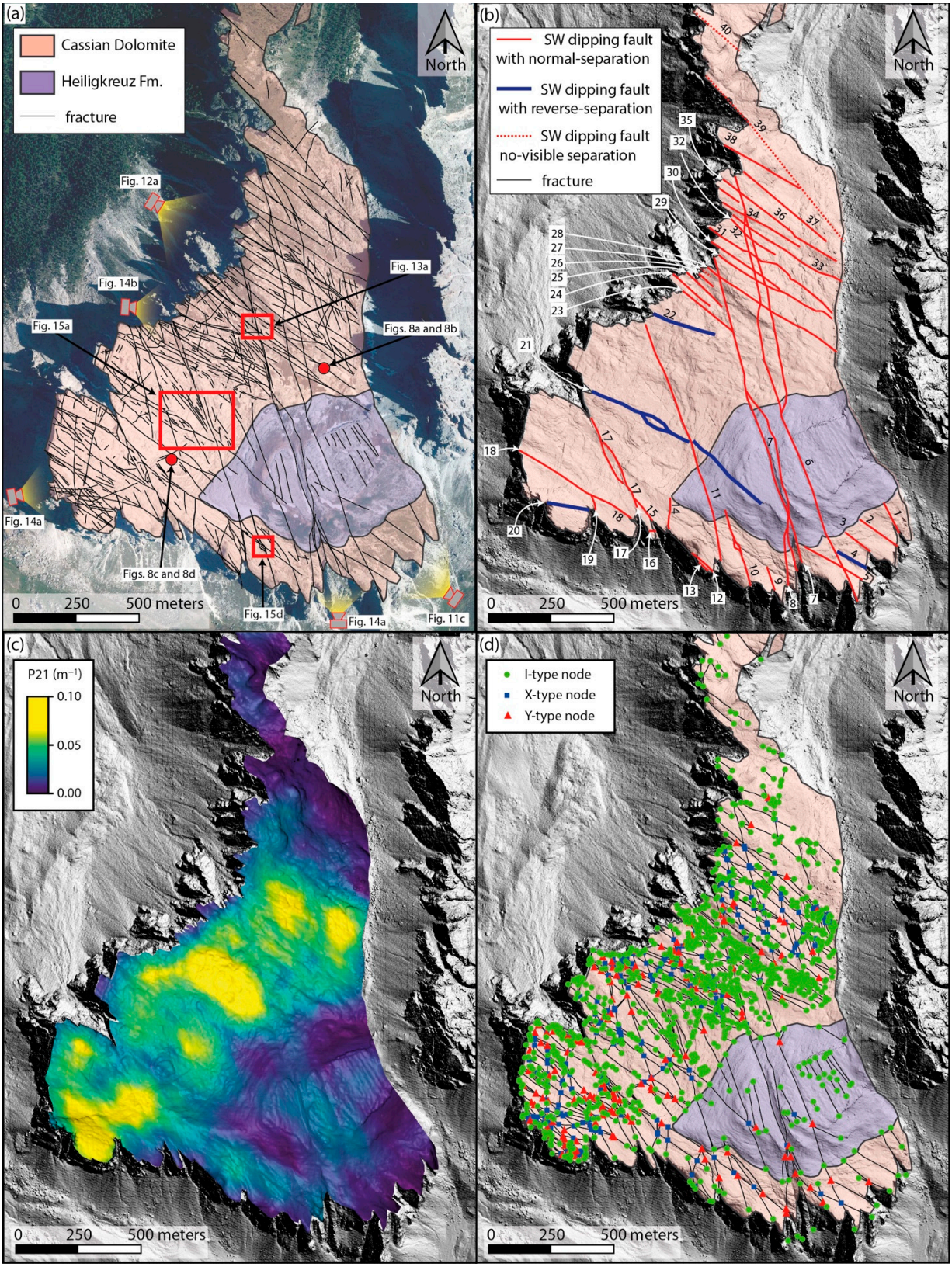

Figure 5. Orthorectified view of the analysis of (**a**) fracture orientation, (**b**) fracture displacement/kinematic, (**c**) fracture areal intensity (P21)., and (**d**) fracture network topology. The AGEA2012 orthoimage and 1 m resolution LiDAR DEM used as background are retrievable from [28].

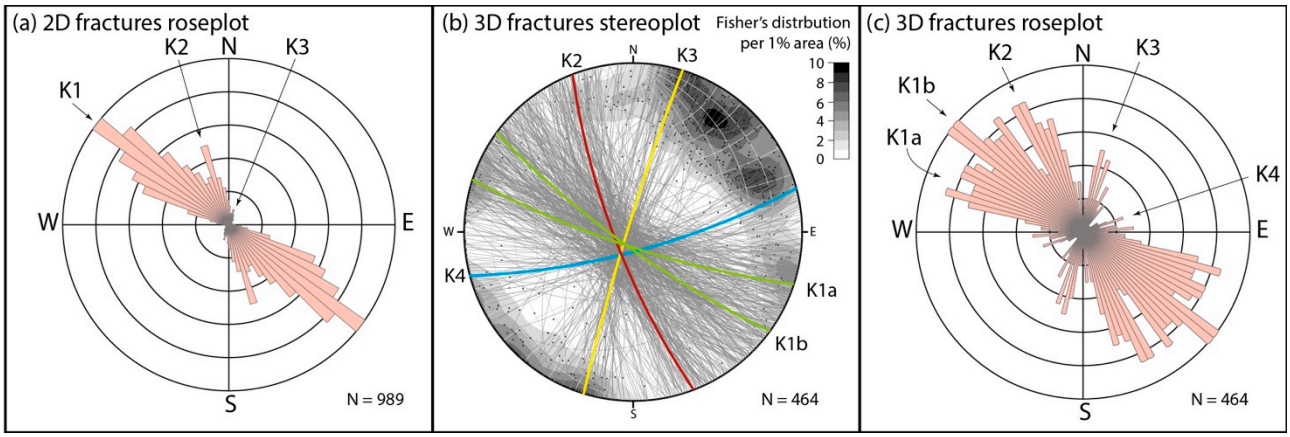

Figure 6. (**a**) Length-weighted roseplot of the 2D fracture trace trend, (**b**) stereoplots, and (**c**) roseplot of the 3D fracture planes attitude and trend. The stereoplot (lower hemisphere equal angle projection) shows the attitude of the mean plane of the recognized fracture sets K1a, K1b, K2, K3 and K4.

The 3D and 2D mapping show similar results, indicating the presence of the same sets, K1, K2, and K3. Notwithstanding, the 3D mapping reveals the presence of a fourth set, K4, that cannot be clearly identified by the mapped 2D fracture traces and allows us to distinguish the sub-set K1a and K1b. Upon classifying the 2D fracture traces according to the 3D results (e.g., Figure 6c), it has been possible to assign 614, 248, 103, and 24 fractures to K1 (176 K1a and 438 K1b), K2, K3, and K4, respectively. According to this classification, the analyses of the 2D fracture trace length (Figure 7a) and 3D fracture plane size (Figure 7b) show a similar fracture size distribution, indicating that K1 and K2 have the largest dimensions.

Despite these similarities, the 2D and 3D datasets show some differences in the general distribution of the trace size. The size distribution of the 2D dataset is characterized by minimum and maximum values of ca. 4 m and 1184 m, a mean length of ca. 89 m (standard deviation of ca. 122), and a mode ranging between 20 and 30 m, while the 3D data are characterized by minimum and maximum values of ca. 2 m and 291 m, a mean length of ca. 36 m (standard deviation of ca. 40), and a mode ranging between 10 and 20 m. While the maximum sizes of the 2D and 3D fracture datasets are conditioned by the extension of the Lastoni di Formin outcrop of the orthoimage and the height of the cliffs, respectively, the minimum size of both fracture datasets is due to the resolution and the fracture sampling strategies. As shown by [67] for the 2D datasets, the 'effective' fracture mapping resolution is at least twice that of the orthoimage resolution, and for the 3D dataset, fractures under 2 m size were considered not important for the 3D analysis of the fracture attitude.

The fracture trend analysis performed at a smaller scale in selected digital scan areas on the DOM-based high-resolution orthoimage of the outcrop summit plateau (e.g., Figure 8a,b) and the field measurements already presented by [1] (e.g., Figure 8c,d) show similar results.

Despite the limitations of the rectangular scan window approach [68], during the analysis of the high-resolution orthoimage, we decided to be consistent with the approach used in the previous study [1]. Due to the aims of this analysis consisting of the comparison between fracture networks of the Cassian Dolomite and Heiligkreuz Fm., the limitations of the rectangular scan window approach can be considered negligible because it affects the two formations and the two sampling scales (field scale, DOM scale) as well.

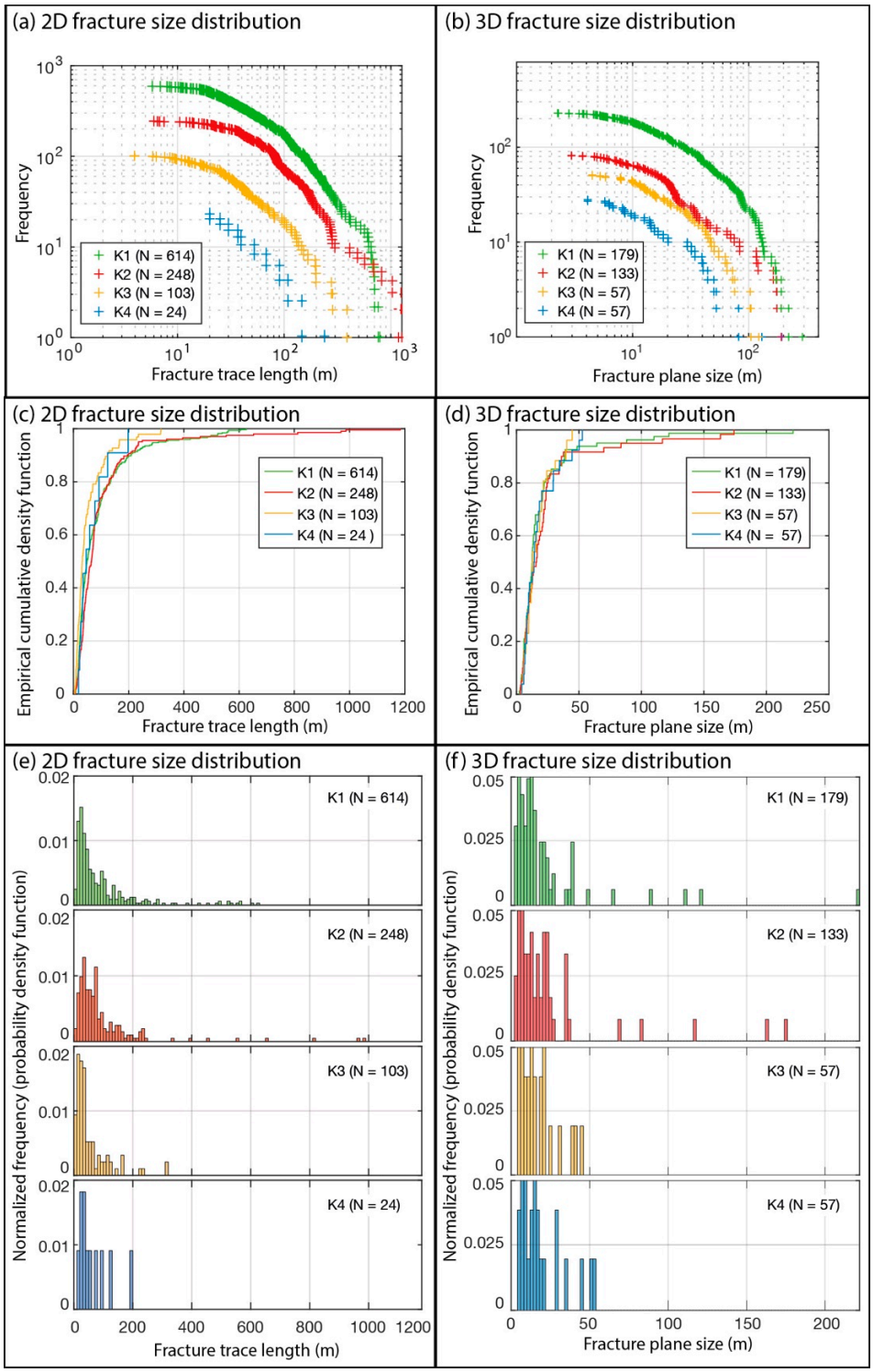

Figure 7. (**a**) Log-log plot, (**c**) empirical cumulative density function plot, and (**e**) normalized histograms (bin size 10 m and normalized by probability density function) of the 2D fracture trace length. (**b**) Log-log plot, (**d**) empirical cumulative density function plot, and (**f**) normalized histograms (bin size 2 m and normalized by probability density function) of the 3D fracture plane size frequency distribution. The sizes of the histograms were selected in order to better represent the fracture trace length and plane size distributions, considering the minimum and maximum values and the resolution of the data. 3D bin size is one order lower than 2D bin size.

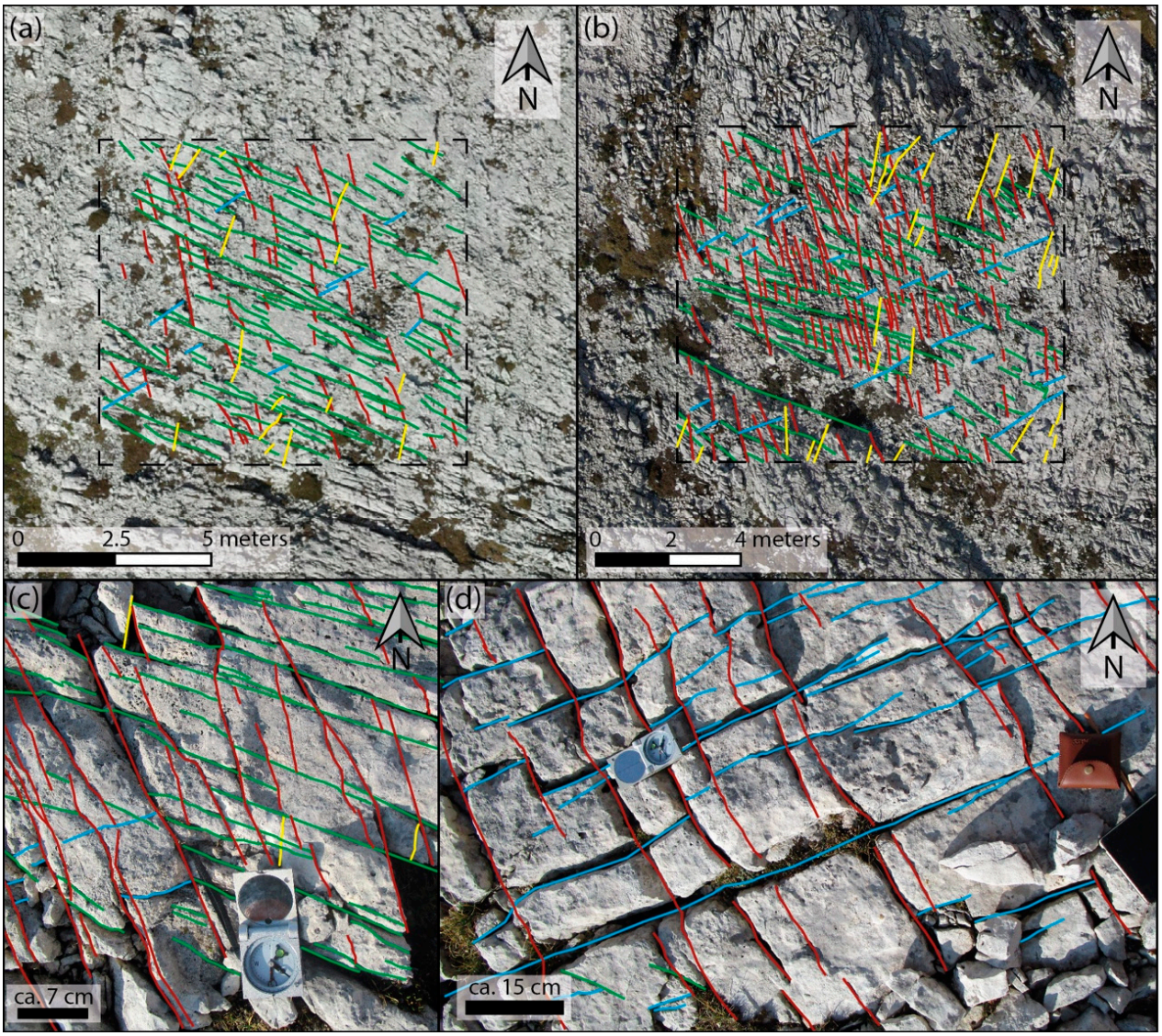

Figure 8. (**a**,**b**) Examples of scan-windows analysis performed using the highest-resolution (2 cm) DOM. (**c**,**d**) Examples of fractures mapped in the field during the rectangular-window scanning. K1, K2, K3, and K4 fractures are marked by green, red, yellow, and light blue traces, respectively.

The analysis confirms that the fracture network is mainly formed by two sets of conjugate fractures, K1 and K2, which resemble the orientation of the major faults and intersect each other with an angle ranging between 45° and 60°, and by two other less frequent sets of fractures, K3 and K4. Generally, field-scale fractures display straight trends and plane parallel matching walls (Figure 8c,d). Moreover, this analysis allowed the careful evaluation of the possible differences between the fracture networks affecting the Cassian platform and the overlying the Heiligkreuz Fm. From the DOM analysis, 2685 and 818 fracture traces were collected on the scan areas of the Cassian Dolomite and Heiligkreuz Fm., respectively. The fracture traces of the Cassian Dolomite are characterized by minimum and maximum trace lengths of ca. 7 cm and 8.34 m and a mean length of ca. 75 cm (standard deviation of ca. 70 cm), whereas the fracture traces of the Heiligkreuz Fm. are characterized by minimum and maximum lengths of ca. 14 cm and 10.53 m and a mean length of ca. 1.43 m (standard deviation of ca. 1.10 m) (Figure 9).

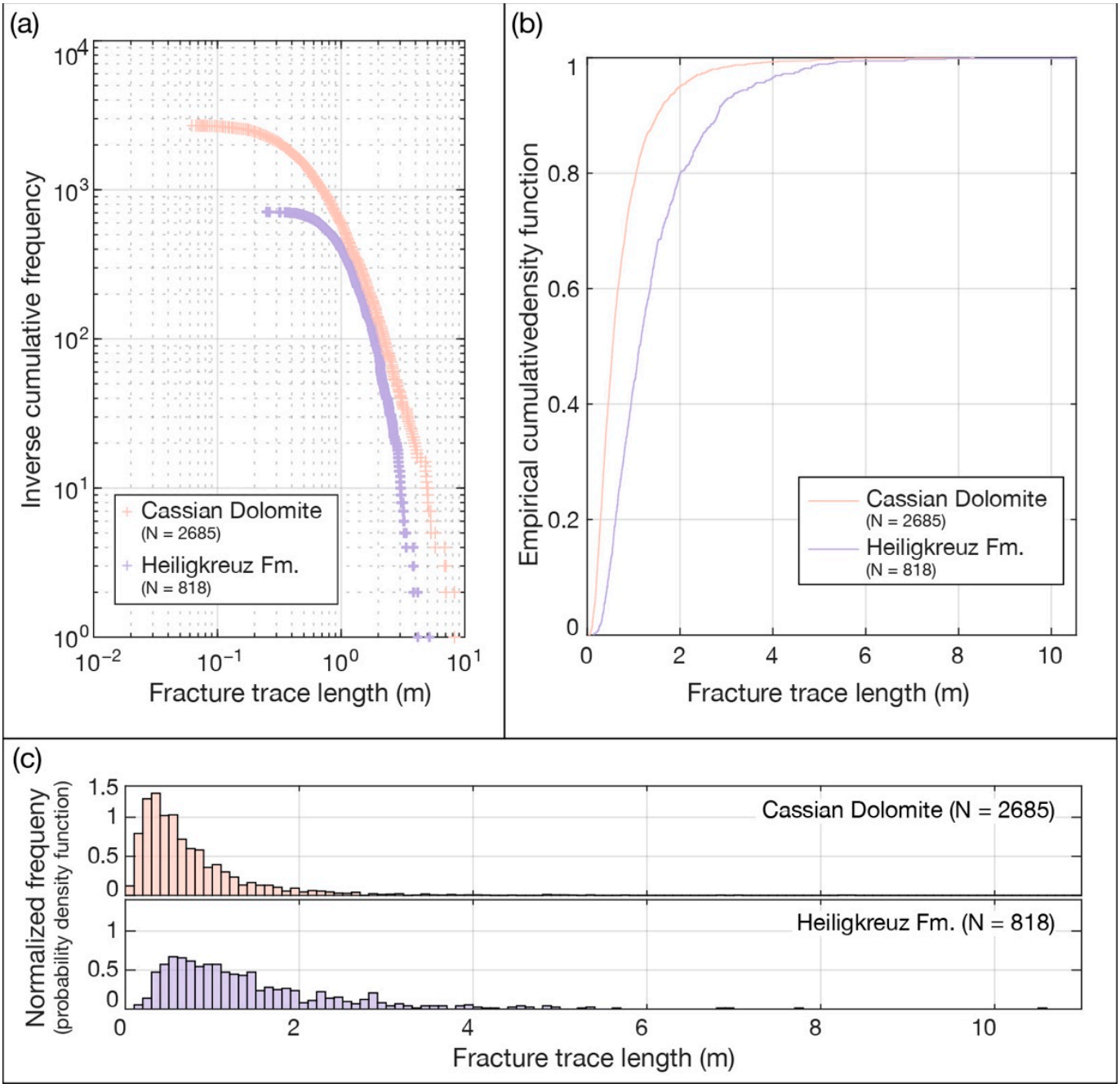

Figure 9. (**a**) Inverse cumulative frequencies, (**b**) empirical cumulative density function, and (**c**) normalized histograms (bin size 10 cm and normalized by probability density function) of the length of fracture traces mapped onto the digital scan areas analyzed onto the Cassian Dolomite and Heiligkreuz Fm.

The results of the comparison of the fracture trend analysis at two different scales (Figure 10) clearly show that the K2 set, trending at 150–160° N, is present in both the Cassian Dolomite and Heiligkreuz Fms., whereas the K1 set, trending at 110–130° N, is present only in the Cassian Dolomite and is substantially absent in the Heiligkreuz Fm.

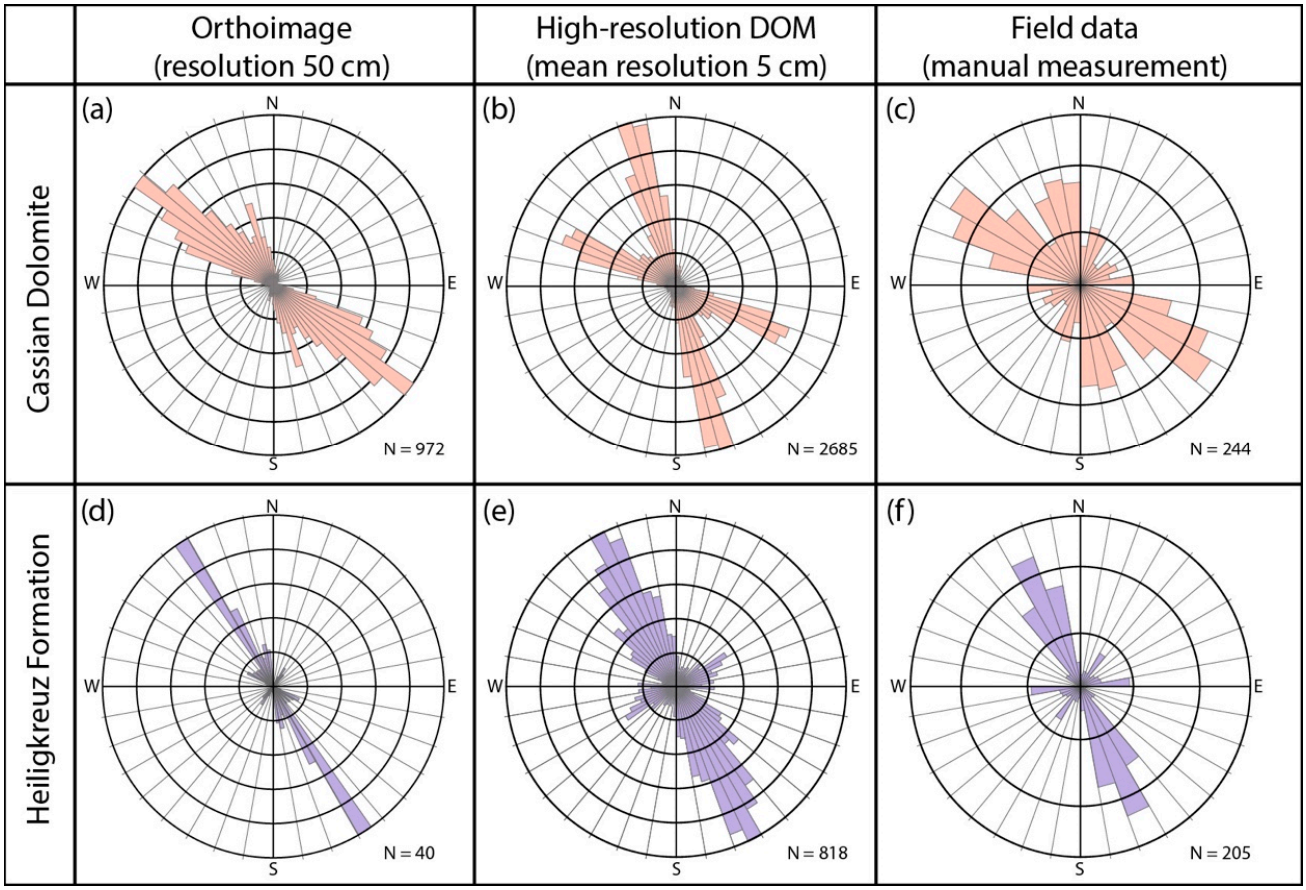

Figure 10. Comparison of the trends of fractures mapped in 2D on the top surface of Cassian platform (**a**–**c**) and on the overlying Heiligkreuz Fm (**d**–**f**). Fractures were mapped from the orthoimage (**a**,**b**), high-resolution DOM (**b**,**e**), and directly on the outcrop (**c**,**f**) during the field survey. The roseplots represent the logarithmic frequency for bin size of 10°.

The comparison based on the high-resolution DOM-orthoimage strongly confirms the results presented by [1] and is based only on field data, revealing a strong prevalence of K2 structures at the top of the Heiligkreuz formation with respect to K1 structures. These latter structures, widely outcropping on the Cassian platform pavements, are much less frequent in the overlying Heiligkreuz Fm deposited after the demise of the Lastoni di Formin buildup.

4.2. Fracture Displacement and Kinematics

This analysis was performed by inspecting the 3D fracture dataset and the 3D line-drawing. The latter was used to correlate all the visible strata along the outcrop cliffs (Figure 11a,b), identify the main faults, and quantify their visible stratigraphic separation (Figure 11c).

During the DOM-based inspection of the outcrop, 40 faults were detected, and the stratigraphic separations of 37 of them were estimated by using the 'Measure two-points thickness' tool of the Compass plugin [66] and measuring the bedding-orthogonal distance between correlated layers on the opposite side of the sliding surface (Table 2).

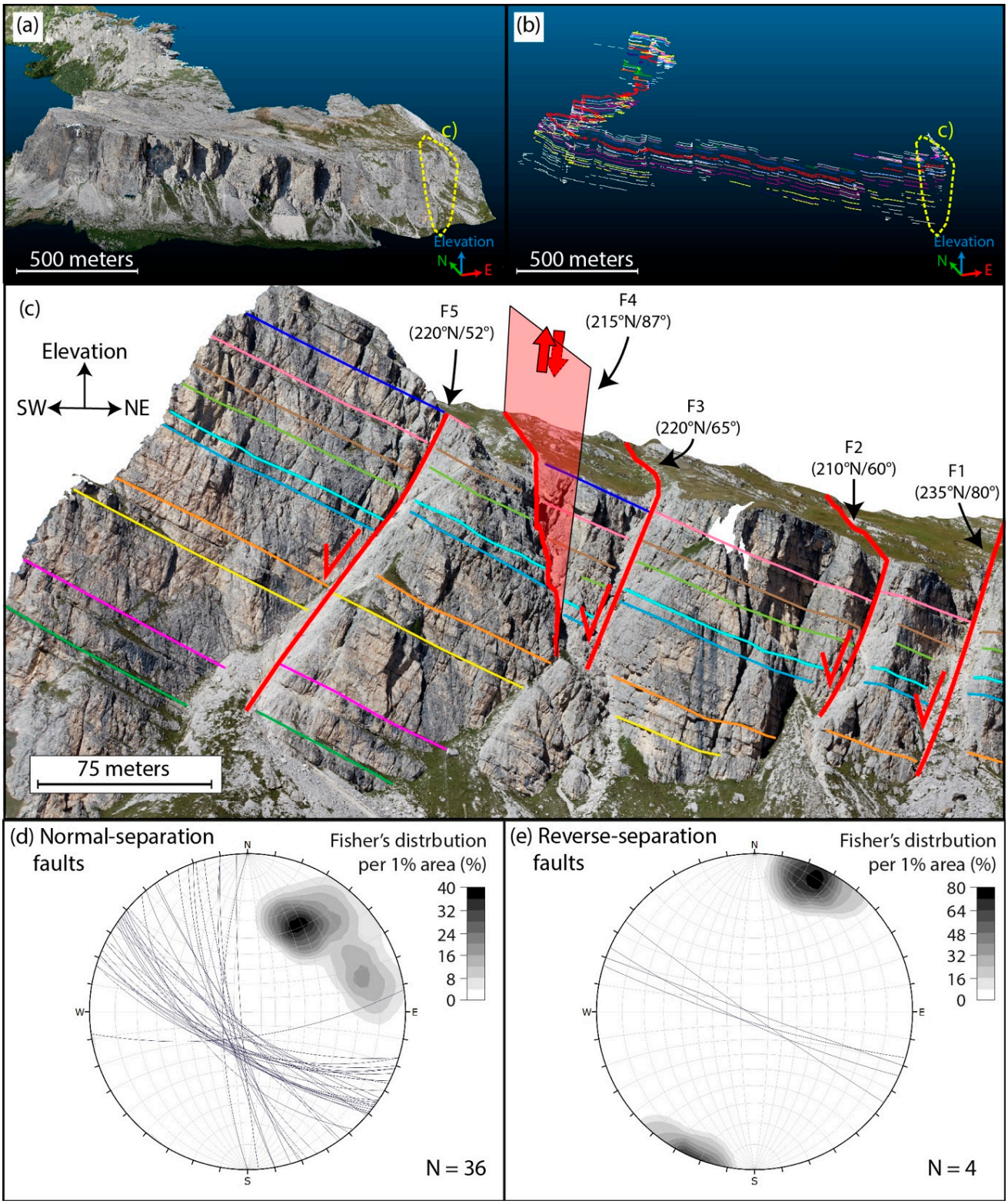

Figure 11. (**a**) Bird's eye view toward NE of the 3D DOM and (**b**) 3D line-drawing of the visible stratigraphic horizons. (**c**) Horizontal and orthographic view toward NW of the 3D DOM where the faults and the strata are highlighted (see Figure 5b for the fault location). F1, F2, F3, and F5 show normal stratigraphic separation, whereas F4 shows an inverse separation. (**d**) Normal- and (**e**) reverse-separation faults stereographic projection (lower hemisphere equal).

Table 2. Fault orientation and stratigraphic separation.

Fault Number	Dip Direction (°N)	Dip (°)	Stratigraphic Separation		
			Type	Mean Value (m)	N. of Measures
1	235	80	normal	7.7	2
2	210	60	normal	7.2	4
3	220	65	normal	15.9	3
4	215	87	reverse	9.3	7
5	220	52	normal	11.9	9
6	270	72	normal	18.8	9
7	250	70	normal	31.2	3
8	260	78	normal	18.9	3
9	248	70	normal	11.0	8
10	244	69	normal	2.1	7
11	260	75	normal	4.3	5
12	220	75	normal	3.9	5
13	230	70	normal	4.4	6
14	266	85	normal	3.8	7
15	234	81	normal	4.3	7
16	172	72	normal	7.0	7
17	254	80	normal	9.0	6
18	213	79	normal	5.0	12
19	251	76	normal	2.3	2
20	204	81	reverse	19.3	4
21	200	89	reverse	1.1	5
22	197	82	reverse	5.0	2
23	218	63	normal	6.1	12
24	217	63	normal	9.4	4
25	215	59	normal	4.5	5
26	200	64	normal	7.2	3
27	216	60	ND	ND	0
28	201	60	normal	7.7	1
29	214	59	normal	13.2	1
30	207	72	normal		
31	203	63	normal	3.6	4
32	201	62	normal	2.4	2
33	215	79	normal		
34	206	65	normal	3.2	3
35	206	65	normal	1.8	3
36	219	62	normal	4.4	5
37	221	81	normal	2.3	3
38	197	70	normal	6.5	11
39	228	53	ND	ND	0
40	197	62	ND	ND	0

Two main sets of normal stratigraphic separation faults are visible. They are likely extensional faults that are hundreds of meters long and cross the entire volume of the outcrop with a mean attitude of 210° N/64 ° (K1) and 250° N/75° (K2). Due to the lack of kinematic indicators, it cannot be excluded that some of these normal-separation faults are strike-slip faults or have been reactivated with strike-slip kinematics. The ascertained strike-slip structures affecting Lastoni di Formin will be presented and discussed further.

K1 faults are particularly well exposed in the central part of the western cliff of Lastoni di Formin; they display a listric geometry and a small normal stratigraphic throw toward SW. They present branches and conjugate faults and are arranged in a regularly spaced domino array (Figure 12a).

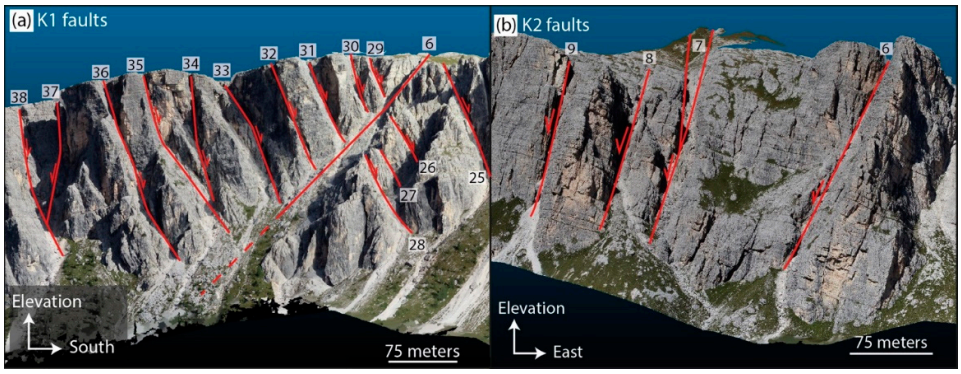

Figure 12. (**a**) Horizontal view toward east of the DOM representing the central part of the western cliff of Lastoni di Formin where the K1 faults are visible. (**b**) Horizontal view toward north of the DOM representing the eastern part of the Lastoni di Formin south wall where the main K2 faults (fault segments 7 and 8) are visible.

K2 faults show a higher inclination (approximately 75°) and a dip direction toward W. The main K2 fault (fault segments 7 and 8) dissects both the Cassian dolomite and the overlying Heiligkreuz formation (Figure 12b). This fault splits into three branches corresponding to the south wall of the outcrop, where a displacement of more than 30 m on the main branch (fault 7) can be measured. Both K1 and K2 structures form large trenches at the fault core (1 m ca. Figure 13), sealed by soils and loose carbonate material.

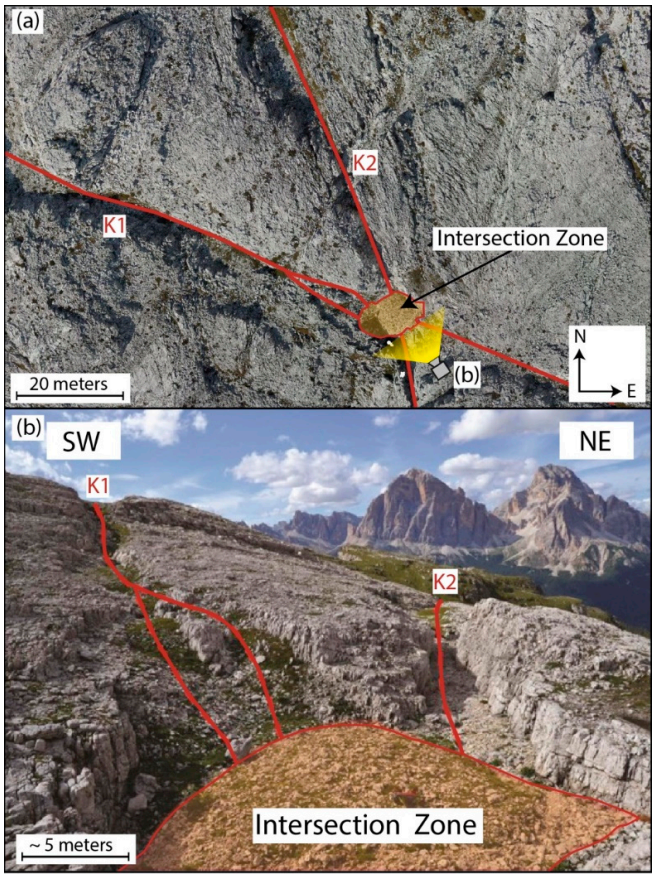

Figure 13. Trenches at the fault core and intersection zone of K1 and K2 faults on the top of the Lastoni di Formin platform as it appears in the UAV-photographs (**a**) and in the field (**b**). Note the large trenches that characterize the fault core and the depression zone formed at the intersection between the two faults.

In the field, the fault and fracture surfaces are strongly altered by pervasive dolomitization and weathering, preventing the recognition of kinematic indicators, such as slickenlines and calcite slickenfibers. However, evidence of strike-slip deformation affecting the platform was detected on DOM by observing the geometrical features of several fractures. In particular, several nearly vertical faults with no visible stratigraphic separation and a mean orientation of N202°/87° (Figure 11e) are clearly visible along the west cliff, which crosscut and slightly displace the older K1 fault planes (Figure 14).

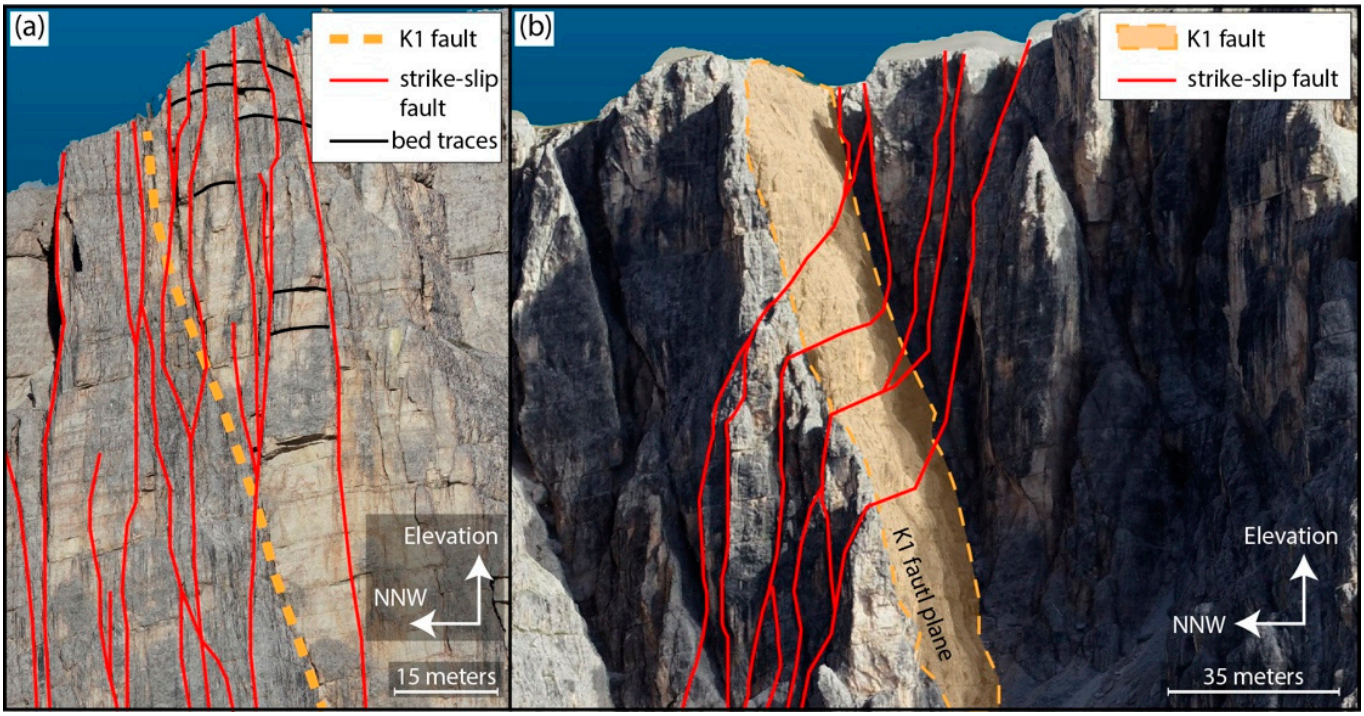

Figure 14. (**a**) Sub-vertical strike-slip faults that crosscut a K1 fault near Forcella Giau. The combination of strike-slip and compression generates an uplifted antiformal "dome" that forms the peak of Lastoni. (**b**) Detail of sub-vertical faults that crosscut a K1 fault plane along the western cliff of the outcrop.

Near Forcella Giau narrow shear fractures, characterized by reverse stratigraphic separation, generate an uplifted antiformal area on the top surface (Figure 14a).

The DOM-based morphometric analysis of the top plateau of Lastoni di Formin reveals that K1 and K2 faults often form pull-apart-like zones of depression in which confined fractures form a 30° angle with the faults (Figure 15a–c). These faults often show conjugate geometry by intersecting themselves with an angle of 40–50° (Figure 15d); in this area, several mode-I fractures are parallel to the bisector of these faults.

4.3. Fracture Intensity

The analysis of the fracture intensity was performed at the top of the Lastoni di Formin using the DICE algorithm, developed by [69] and retrievable from [70]. Following the guidelines of [69], the scan radius of the scan circular window was set as ca. 90 m. The DICE-based analysis shows that the Cassian Dolomite has a higher fracture intensity with respect to the Heiligkreuz Fm. (Figure 5c). The fracture intensity is essentially due to the K1b set because it is more frequent (NK1b = 438; 44.3%) with respect to K1a (NK1a = 176; 17.8%), K2 (NK2 = 248; 25.1%), K3 (NK3 = 103; 10.4%), and K4 (NK4 = 24; 2.4%). This could explain the relatively low fracture intensity of the Heiligkreuz Fm., which is substantially free of K1 fractures.

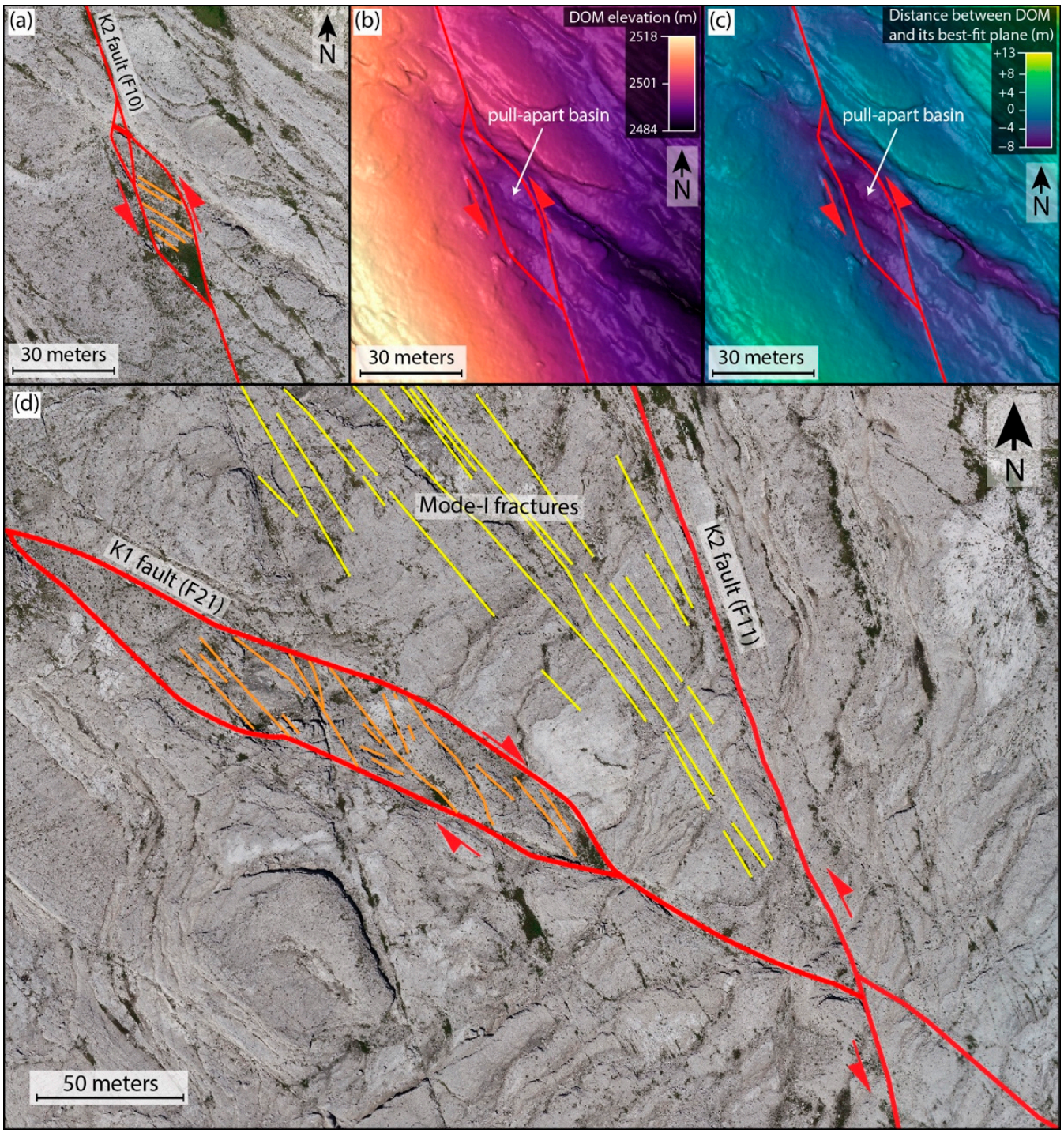

Figure 15. Examples of strike-slip structures visible at the top of the platform. (**a**) DOM top view of a releasing stepover structure that forms a sort of small pull-apart basin along a K2 fault. Its presence is enhanced by (**b**) the DOM elevation and (**c**) the DOM distance from the 'local' plane that best fits the surface of the top plateau. (**d**) Releasing stepover on a K1 fault (F11) and mode-I (tensional) fractures oriented parallel to the bisector of the conjugate strike-slip faults. The inferred kinematics is dextral for the K1 and sinistral for the K2 faults, respectively.

In the Cassian Dolomite, at the field-scale, fractures show an increase in their intensity toward the faults [69].

4.4. Fracture Network Topology

A topological analysis of the fracture network (sensu [71]) affecting both the Cassian Dolomite and Heiligkreuz Fm. was performed using the Network-GT plugin of QGIS. The results of this analysis are displayed in Figure 16 and reported in Tables 3 and 4.

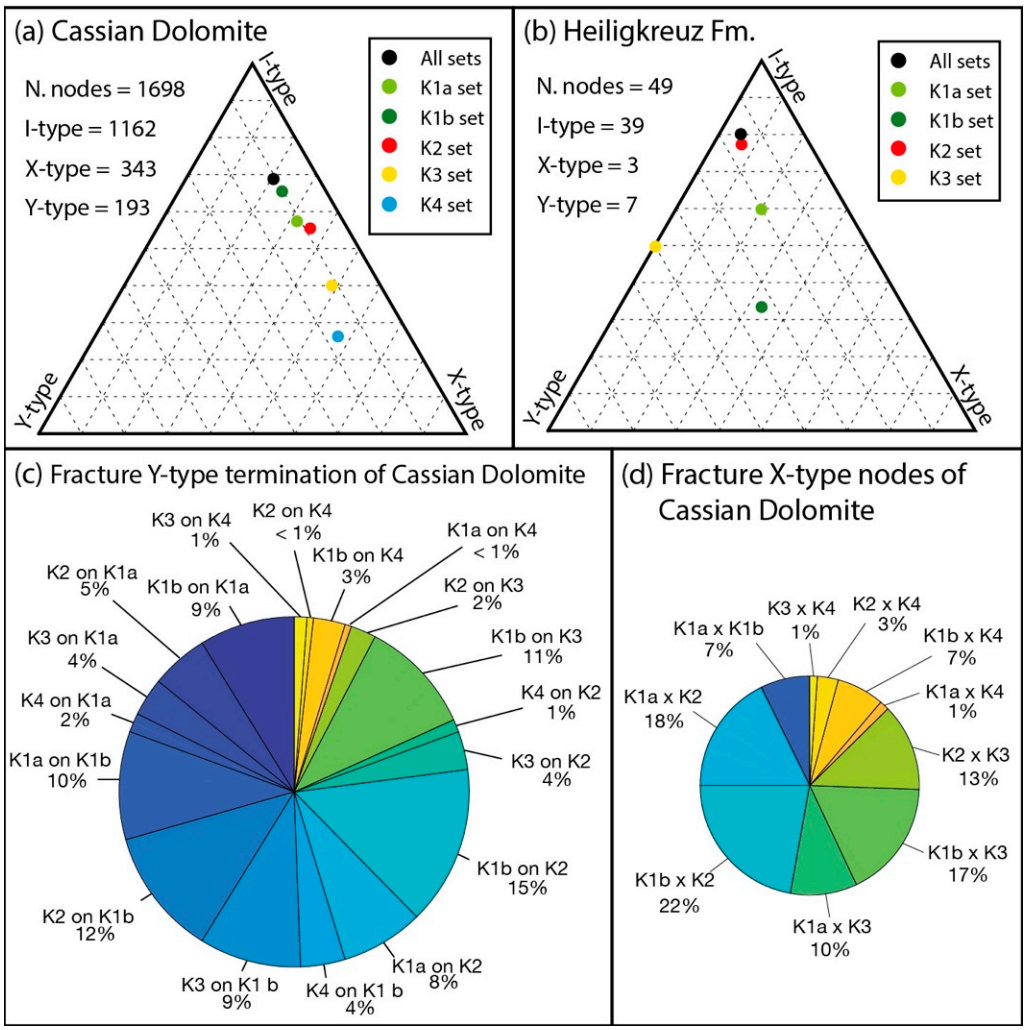

Figure 16. Ternary plots of the fracture termination nodes and branches defining the 2D fracture network topology for (**a**) Cassian Dolomite and (**b**) Heiligkreuz Formation. Pie-charts representing (**c**) the proportion of Y-type termination (fracture terminates on fracture) and (**d**) X-type nodes of the fracture network topology of Cassian Dolomite.

Table 3. Fracture nodes statistic retrieved from the topological analysis of the 2D fracture traces mapped onto the top of Lastoni di Formin Cassian Dolomite.

Set	Nodes		
	I-Type	X-Type	Y-Type
All sets	1162 (68%)	343 (20%)	193 (12%)
K1a	219 (59%)	120 (32%)	35 (9%)
K1b	492 (66%)	183 (24%)	74 (10%)
K2	317 (57%)	199 (36%)	41 (7%)
K3	114 (40%)	141 (49%)	30 (11%)
K4	20 (27%)	42 (56%)	13 (17%)

Table 4. Fracture node statistics retrieved from the topological analysis of the 2D fracture traces mapped onto the top of Lastoni di Formin Heiligkreuz Fm.

Set	Nodes		
	I-Type	X-Type	Y-Type
All sets	39 (80%)	3 (6%)	7 (14%)
K1a	3 (60%)	1 (20%)	1 (20%)
K1b	1 (33%)	1 (33%)	1 (33%)
K2	34(77%)	3 (7%)	7 (16%)
K3	1 (50%)	0 (0%)	1 (50%)
K4	-	-	-

The overall topology of the fault and fracture network (see also a preliminary analysis in [1]) affecting the Cassian Dolomite (I-nodes 68%, X-nodes 20%, and Y-nodes 11%) is mainly influenced by K1b (I-nodes 66% X-nodes 24%, and Y-nodes 10%) and secondly by K1a (I-nodes 59%, X-nodes 32%, and Y-nodes 9%) and K2 nodes (I-nodes 57%, X-nodes 36%, and Y-nodes 7%), whereas K3 and K4 show a slightly different topology (I-nodes 40%, X-nodes 49%, and Y-nodes 11% for K3 and I-nodes 27%, X-nodes 56%, and Y-nodes 17% for K4). In general, most of the abutting relationships (Y-type nodes; Figure 12c) regard fractures abutting against the K1 set (55%), especially against the K1b subset (33%). Fractures that abut against K2 are also relatively abundant, representing ca. 28% of all Y-type terminations. Fractures that abut against K3 and K4 are the least abundant, representing less than 19% of all Y-type terminations.

The topology of the fracture network affecting the Heiligkreuz Fm. is quite different (I-nodes 80%, X-nodes 6%, and Y-nodes 14%) and seems to be mostly influenced by K2 (I-nodes 77%, X-nodes 7%, and Y-nodes 16%) and successively by K1a (I-nodes 60%, X-nodes 20%, and Y-nodes 20%), whereas K3 and K1b show a slightly different topology (I-nodes 50%, X-nodes 0%, and Y-nodes 50% for K3 and I-nodes 33%, X-nodes 33%, and Y-nodes 33% for K1b). Notwithstanding this, due to the low number of fracture nodes detected, the results of the topological description of the fracture network affecting the Heiligkreuz Fm. must be considered only qualitatively.

5. Discussion

Relative Timing and Deformation History

The analysis of the orthoimage, LiDAR aerial dataset, and UAV-based DOM, together with the results of field observations, provide valuable information on the relative timing of the different fracture sets affecting the carbonate platform. The results confirm the findings of [1,2] that several ESE-WNW-trending K1 extensional fractures and normal faults occurred during or shortly after the platform growth due to the differential compaction of the basinal unit driven by the platform progradation and aggradation [1,2] and predate the tilting of the platform and further tectonic events that generated other structures. The K1 normal faults are characterized by a metric normal stratigraphic separation and have extensively affected the Cassian Dolomite, lowering the platform interior (Figures 5b, 11d and 12a). These faults that dip towards the inner platform are possible due to the differential compaction of the San Cassiano basinal Formation that may have induced a greater lowering of the sectors towards the aggrading inner platform [1,2]. Regarding field-scale fractures (Figure 10), they are substantially absent in the overlying Heiligkreuz Fm. (Figure 5c). This helps to limit their origin to a moment before the deposition of this unit: K1 fractures were likely formed during or shortly after the platform growth (Late Ladinian, Early Carnian). This hypothesis is also supported by the analysis of the topological relationships between fractures (Figure 16), as generally most of the K2, K3, and K4 fractures terminate against the K1 fractures, especially K1b, suggesting an earlier relative timing of K1 and their synsedimentary age [1]. K1 fractures were generated by the differential subsidence of the basinal deposits located at the platform margin under

the load of the prograding platform [1,2], so due to their synsedimentary origin they can be associated with an early embrittlement phase of carbonate rocks [13] and they could have played a significant role in the early diagenetic fluid migration, triggering karst development and enhanced permeability [72–76].

However, it should be noted that some of the K1 fractures may have a more recent origin because they do not display synsedimentary features, are nearly vertical, and show right-hand strike-slip displacement (Figure 15d). The analysis of the altitude of the reverse stratigraphic separation faults (Figure 11e; Table 2) clearly suggests that most of the newest K1 and/or reactivated ones may belong to the subset K1a due to their comparable orientation.

NNW-SSE K2 fractures, on the other hand, are widespread both in the Cassian Dolomite and Heiligkreuz Fm. and post-date K1 structures. Taking into account their orientation (Figure 6) and extensional kinematics (Figures 11d and 12b), we suggest that this set is possibly related to the E-W phase of extension and rifting that occurred in the Dolomites during Upper Triassic–Jurassic times. The analysis of the fracture network topology supports this hypothesis, showing that K2 directly follows K1 in terms of fractures that terminate against it, and suggests that most of the potential fracture network conductivity is developed, showing that most of the connection nodes (e.g., X- and Y-type nodes) relate to fracture sets K1 and K2.

The last phases of deformation that affected the area during the Alpine Orogeny are responsible for the partial reactivation of the preceding K1 and K2 structures, the formation of new parallel fractures, and the genesis of K3 and K4 fractures. The more recent genesis of K3 and K4 fractures has also been shown by the analysis of the fault and fracture traces (Figure 7), which indicates that the traces of K3 and K4 are generally shorter than those of K1 and K2 and that the larger part of the Y terminations are due to K1 and, subordinately, younger fractures (e.g., K3), which abut against the older ones (K2) (Figure 16).

Strike-slip kinematics is likely the more relevant manifestation of these last phases of deformation. In general, due to the lack of clear fault surface kinematic indicators, the shear sense was inferred by the geometries of structures (e.g., [13,77,78]). Extensional releasing stepovers form small local zones of depression, often partially filled with detritic materials or soil. In contrast, restraining compressional stepovers produce local shortening that generates uplifted areas that are, however, usually partially eroded and, therefore, more difficult to recognize. The linkage of the parallel fault segments generally occurs through the development of R and P fractures. According to this rationale, the observations revealed dextral kinematics for the subvertical, nearly E-W-trending faults (parallel to K1 fractures, Figure 14a) and sinistral strike-slip reactivation for the inherited K2 faults (Figure 15). However, the presence of some indicators such as releasing bands suggests that some K1 normal faults were also subjected to dextral reactivation (Figure 15d).

Therefore, it can be supposed that a strike-slip tectonic regime, characterized by an NW-SE maximum compressional axis, generated new 100–120° N-trending right strike-slip faults and K3 sinistral strike-slip structures that intersected the preceding/inherited extensional K1 and K2 fractures and faults. This hypothesis is also supported by the releasing stepover structures detected in the study area, which suggest reactivation with a sinistral-offset strike-slip kinematic of westward-dipping K2 normal faults (Figure 15a–c), and by the conjugate arrangements of K1 and K2 strike-slip faults and mode-I fractures (Figure 15d).

Similar releasing stepover structures at a larger scale were reported for Croda da Lago—Rocchette and Col di Gallina structures, where K2-trending strike-slip structures are associated with normal faults with huge dimensions and offsets and opposite vergence that develop pull-apart basins [26,30].

K4 fractures were likely generated as compressional fractures with a direction sub-orthogonal to the maximum compressional axis. These features, similar to those reported by [79] on the coeval Cassian platform of the Sella Complex, are consistent with the NW-SE direction of the maximum compressive stress during the last phases of the Alpine compres-

sions and the consequent kinematic inversion of the pre-existent structures inherited from the earlier tectonic phases. Lastly, considering the orientation of the K3 and K4 fractures, it cannot be excluded that the Alpine compressional phase of deformation could have been characterized during the Neogene by an anticlockwise reorientation of the maximum compressional axis from N-S (or NNE-SSW) to NW-SE.

The sketch in Figure 17 summarizes the major deformational phases that affected the platform and the resulting structural features.

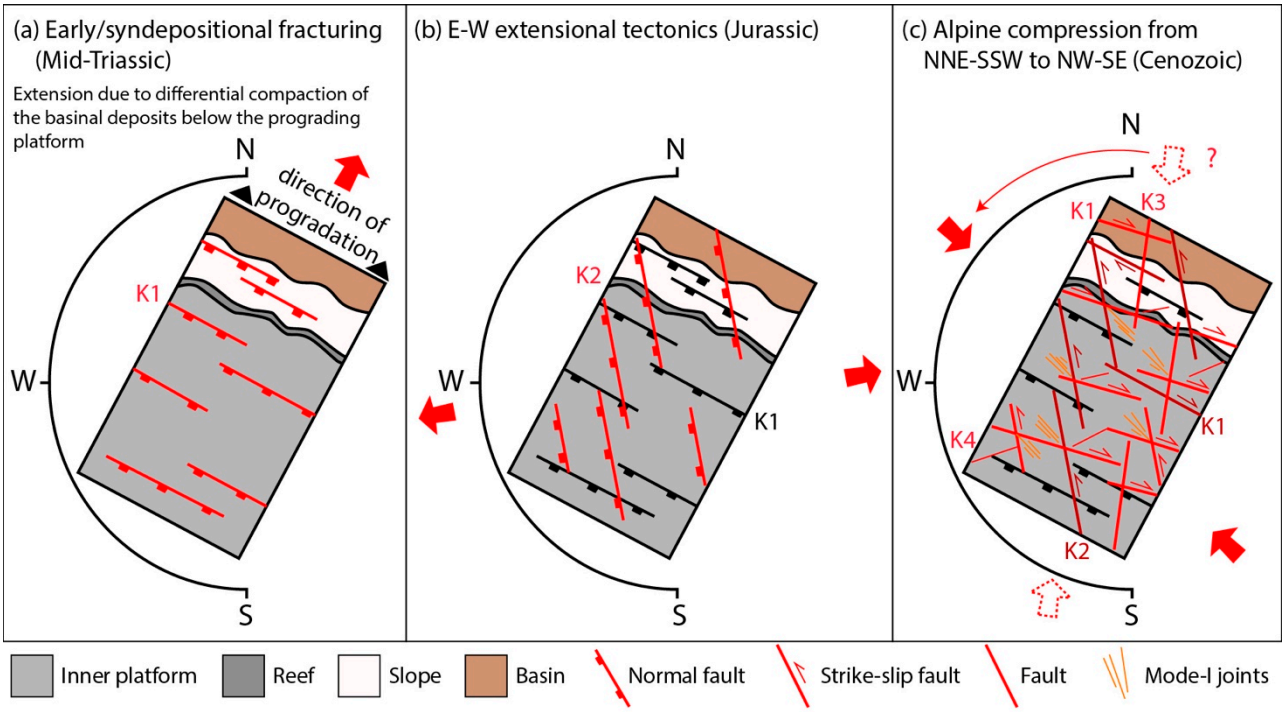

Figure 17. Sketch of the main deformational phases that affected the platform of Lastoni di Formin: (**a**) K1 faults and fractures formation due to the early/syndepositional fracturing driven by differential compaction processes; (**b**) K2 faults and fractures formation due to the Jurassic E-W extensional tectonics; (**c**) K1 and K2 fault and fracture reactivation and K1, K3, and K4 faults and fractures formation due to the NNE-SSW to NW-SE Alpine compression (Cenozoic).

6. Conclusions

The complex fracture and fault network that affects the Lastoni di Formin platform is the result of several overlapping deformational events that occurred essentially in a brittle regime. Most of the mapped structures correspond to fractures, and the faults detected along the platform seem to accommodate little strain, showing relatively small metric displacements (except the main K2 fault that displays a normal stratigraphic offset of ~20 m, clearly dissecting the Heiligkreuz Formation). Considering the features and the geometry of the detected fractures, the main deformational events that affected the platform can be summarized as follows:

1. Compaction-induced deformation that generated WNW-ESE-trending K1 extensional fractures and normal faults, perpendicular to the direction of platform progradation, likely active during or shortly after the platform growth (Late Ladinian, Early Carnian).
2. Extensional tectonics, likely related to the Jurassic rifting phase, led to the formation of NNW-SSE striking K2 fractures and westward-dipping normal faults.
3. Neogene compressional tectonics, characterized by an N-S to NW-SE crustal shortening that deformed the platform essentially with fractures and strike-slip structures: The best-documented deformational phase is characterized by an NW-SE-trending maximum compressional axis and is associated with the formation of new 100–120° N-

trending right strike-slip faults and K3 sinistral strike-slip structures that intersected the preceding extensional K1 and K2 fractures and faults. The partial transcurrent reactivation of the preceding K1 and K2 structures together with the generation of new sets of fractures (K3 and K4) suggest that the Neogene strike-slip tectonics could be characterized by a reorientation of the maximum compressional axis from N-S (or NNE-SSW) to NW-SE.

Author Contributions: Conceptualization, N.M., R.I. and C.P.; methodology, N.M., R.I., Y.P. and C.P.; software, N.M., R.I., Y.P. and C.P.; validation, N.M., R.I., Y.P. and C.P.; formal analysis, N.M., R.I., Y.P., M.C. and C.P.; drone flight planning and execution: M.C.; investigation, N.M., R.I., Y.P. and C.P.; resources, N.M., R.I., Y.P. and C.P.; data curation, N.M., R.I., Y.P. and C.P.; writing—original draft preparation, N.M. and R.I.; writing—review and editing, N.M., R.I., Y.P. and C.P.; visualization, N.M., R.I. and Y.P.; supervision, N.M., R.I. and C.P.; project administration, C.P. All authors have read and agreed to the published version of the manuscript.

Funding: This research received no external funding.

Acknowledgments: We would like to thank Silvia Passoni and Manuele Bettoni for their help during the data acquisition and Luca Pizzimenti for their precious advice on the use of the LiDAR data. Francesco Zucca and Silvia Mittempergher are acknowledged for their useful comments and suggestions. Many thanks are given to ENI Spa for the support provided in this study. We would also like to thank Juliet Aber for the non-technical review of the English language.

Conflicts of Interest: The authors declare no conflict of interest.

References

1. Inama, R.; Menegoni, N.; Perotti, C. Syndepositional fractures and architecture of the Lastoni di Formin carbonate platform: Insights from virtual outcrop models and field studies. *Mar. Pet. Geol.* **2020**, *121*, 104606. [CrossRef]
2. Menegoni, N.; Inama, R.; Crozi, M.; Perotti, C. Early deformation structures connected to the progradation of a carbonate platform: The case of the Nuvolau Cassian platform (Dolomites—Italy). *Mar. Pet. Geol.* **2022**, *138*, 105574. [CrossRef]
3. Keim, L.; Schlager, W. Automicrite facies on steep slopes (Triassic, Dolomites, Italy). *Facies* **1999**, *41*, 15–25. [CrossRef]
4. Keim, L.; Schlager, W. Quantitative compositional analysis of a Triassic carbonate platform (Southern Alps. Italy). *Sediment. Geol.* **2001**, *139*, 261–283. [CrossRef]
5. Schlager, W. Benthic carbonate factories of the Phanerozoic. *Int. J. Earth Sci.* **2003**, *92*, 445–464. [CrossRef]
6. Neuweiler, F.; Gautret, P.; Thiel, V.; Lange, R.; Michaelis, W.; Reitner, J. Petrology of Lower Cretaceous carbonate mud mounds (Albian, N. Spain): Insights into organomineralic deposits of the geological record. *Sedimentology* **1999**, *46*, 837–859. [CrossRef]
7. Neuweiler, F.; Bourque, P.A.; Boulvain, F. Why is stromatactis so rare in Mesozoic carbonate mud mounds? *Terra Nov.* **2001**, *13*, 338–346. [CrossRef]
8. Flajs, G.; Vigener, M.; Keupp, H.; Meischner, D.; Neuweiler, F.; Paul, J.; Reitner, J.; Warnke, K.; Weller, H.; Dingle, P.; et al. Mud mounds: A polygenetic spectrum of fine-grained carbonate buildups. *Facies* **1995**, *32*, 1–69. [CrossRef]
9. Guido, A.; Mastandrea, A.; Stefani, M.; Russo, F. Role of autochthonous versus detrital micrite in depositional geometries of Middle Triassic carbonate platform systems. *Bull. Geol. Soc. Am.* **2016**, *128*, 989–999. [CrossRef]
10. Guido, A.; Russo, F.; Miriello, D.; Mastandrea, A. Autochthonous micrite to aphanodolomite: The microbialites in the dolomitization processes. *Geosciences* **2018**, *8*, 451. [CrossRef]
11. Panara, Y.; Menegoni, N.; Carboni, F.; Inama, R. 3D digital outcrop model-based analysis of fracture network along the seismogenic Mt. Vettore Fault System (Central Italy): The importance of inherited fractures. *J. Struct. Geol.* **2022**, *161*, 104654. [CrossRef]
12. Espejel, R.L.; Alves, T.M.; Blenkinsop, T.G. Multi-scale fracture network characterisation on carbonate platforms. *J. Struct. Geol.* **2020**, *140*, 104160. [CrossRef]
13. La Bruna, V.; Lamarche, J.; Agosta, F.; Rustichelli, A.; Giuffrida, A.; Salardon, R.; Marié, L. Structural diagenesis of shallow platform carbonates: Role of early embrittlement on fracture setting and distribution, case study of Monte Alpi (Southern Apennines, Italy). *J. Struct. Geol.* **2020**, *131*, 103940. [CrossRef]
14. McCaffrey, K.J.W.; Jones, R.R.; Holdsworth, R.E.; Wilson, R.W.; Clegg, P.; Imber, J.; Holliman, N.; Trinks, I. Unlocking the spatial dimension: Digital technologies and the future of geoscience fieldwork. *J. Geol. Soc. London.* **2005**, *162*, 927–938. [CrossRef]
15. Bistacchi, A.; Balsamo, F.; Storti, F.; Mozafari, M.; Swennen, R.; Solum, J.; Tueckmantel, C.; Taberner, C. Photogrammetric digital outcrop reconstruction, visualization with textured surfaces, and three-dimensional structural analysis and modeling: Innovative methodologies applied to fault-related dolomitization (Vajont Limestone, Southern Alps, Italy). *Geosphere* **2015**, *11*, 2031–2048. [CrossRef]
16. Bertrand, L.; Géraud, Y.; Le Garzic, E.; Place, J.; Diraison, M.; Walter, B.; Haffen, S. A multiscale analysis of a fracture pattern in granite: A case study ofthe Tamariu granite, Catalunya, Spain. *J. Struct. Geol.* **2015**, *78*, 52–66. [CrossRef]

17. Martinelli, M.; Bistacchi, A.; Mittempergher, S.; Bonneau, F.; Balsamo, F.; Caumon, G.; Meda, M. Damage zone characterization combining scan-line and scan-area analysis on a km-scale Digital Outcrop Model: The Qala Fault (Gozo). *J. Struct. Geol.* **2020**, *140*, 104144. [CrossRef]
18. Doglioni, C. Tectonics of the Dolomites (southern alps, northern Italy). *J. Struct. Geol.* **1987**, *9*, 181–193. [CrossRef]
19. Stefani, M.; Furin, S.; Gianolla, P. The changing climate framework and depositional dynamics of Triassic carbonate platforms from the Dolomites. *Palaeogeogr. Palaeoclimatol. Palaeoecol.* **2010**, *290*, 43–57. [CrossRef]
20. Servizio Geologico d'Italia—ISPRA; Compagnoni, B.; Galluzzo, F.; Bonomo, R.; Capotorti, F.; D'Ambrogi, C.; Di Stefano, R.; Graziano, R.; Martarelli, L.; Pampaloni, M.L.P.; et al. *Carta Geologica alla Scala 1 a 1,000,000*, 5th ed.; SELCA: Firenze, Italy, 2011; Available online: http://sgi.isprambiente.it/milione/milione5ed.html (accessed on 10 January 2022).
21. Bigi, G.; Castellarin, A.; Coli, M.; Dal Piaz, G.V.; Sartori, R.; Scandone, P.; Vai, G.B. *Structural Model of Italy Scale 1:500.000, Sheet 1*; Progetto Finalizzato Geodinamica, C.N.R., Ed.; SELCA: Firenze, Italy, 1990; Available online: https://www.socgeol.it/438/structural-model-of-italy-scale-1-500-000.html (accessed on 10 January 2022).
22. Bigi, G.; Castellarin, A.; Coli, M.; Dal Piaz, G.V.; Vai, G.B. *Structural Model of Italy Scale 1:500.000, Sheet 2*; Progetto Finalizzato Geodinamica, C.N.R., Ed.; SELCA: Firenze, Italy, 1990; Available online: https://www.socgeol.it/438/structural-model-of-italy-scale-1-500-000.html (accessed on 10 January 2022).
23. Brondi, A.; Fuganti, A.; Mittempergher, M.; Murara, G.; Nardin, M.; Rossi, D.; Scudeler Baccelle, L.; Sommavilla, E.; Zirpoli, G. *Note Illustrative della Carta Geologica d 'Italia alla scala 1: 50.000: Foglio 027-Bolzano*; Nuova Tecnica Grafica: Roma, Italy, 1974. Available online: https://www.isprambiente.gov.it/Media/carg/note_illustrative/27_Bolzano.pdf (accessed on 10 January 2022).
24. Brondi, A.; Mittempergher, M.; Panizza, M.; Rossi, D.; Sommavilla, E.; Vuillermin, F. *Note Illustrative della Carta Geologica d 'Italia alla Scala 1: 50.000: Foglio 028-La Marmolada*; Litografia Artisitica Cartografica: Firenze, Italy, 1977. Available online: https://www.isprambiente.gov.it/Media/carg/note_illustrative/28_Lamarmolada.pdf (accessed on 10 January 2022).
25. Costa, V.; Doglioni, C.; Grandesso, P.; Masetti, D.; Pellegrini, G.B.; Tracanella, E. *Note Illustrative della Carta Geologica d'Italia alla Scala 1: 50.000: Foglio 063-Belluno*; Istituto Poligrafico e Zecca dello Stato: Roma, Italy, 1996. Available online: https://www.isprambiente.gov.it/Media/carg/note_illustrative/63_Belluno.pdf (accessed on 10 January 2022).
26. Neri, C.; Gianolla, P.; Furlanis, S.; Caputo, R.; Bosellini, A. *Note Illustrative della Carta Geologica d'Italia. alla Scala 1:50.000: Foglio 029-Cortina d'Ampezzo*; ISPRA: Roma, Italy, 2007. Available online: https://www.isprambiente.gov.it/Media/carg/note_illustrative/29_CortinaAmpezzo.pdf (accessed on 10 January 2022).
27. Gianolla, P.; Morelli, C.; Cucato, M.; Siorpaes, C. *Note Illustrative della Carta Geologica d'Italia alla Scala 1: 50.000: Foglio 016-Dobbiaco*; ISPRA: Roma, Italy, 2018. Available online: https://www.isprambiente.gov.it/Media/carg/note_illustrative/16_Dobbiaco_ita.pdf (accessed on 10 January 2022).
28. Geoportale Nazionale of Ministero dell'Ambiente e della Tutela del Territorio e del Mare. Available online: http://www.pcn.minambiente.it (accessed on 1 August 2022).
29. Preto, N.; Gianolla, P.; Franceschi, M.; Gattolin, G.; Riva, A. Geometry and evolution of Triassic high-relief, isolated microbial platforms in the Dolomites, Italy: The Anisian Latemar and Carnian Sella platforms compared. *Am. Assoc. Pet. Geol. Bull.* **2017**, *101*, 475–483. [CrossRef]
30. Caputo, R. Tettonica Polifasica nei Dintorni di Cortina d'Ampezzo, Dolomiti Orientali. *Rend Online Soc. Geol. Ital.* **2008**, *1*, 57–61. Available online: https://www.researchgate.net/profile/Riccardo-Caputo/publication/285919639_Polyphase_tectonics_in_the_Cortina_dAmpezzo_area_eastern_Dolomites/links/5cf2f816a6fdcc8475fce7cf/Polyphase-tectonics-in-the-Cortina-dAmpezzo-area-eastern-Dolomites.pdf (accessed on 10 January 2022).
31. Leonardi, P. *Le Dolomiti. Geologia dei Monti tra Isarco e Piave*; Manfrini: Rovereto, Italy, 1968; 1021p.
32. Bosellini, A.; Masetti, D.; Neri, C. La geologia del Passo del Falzarego. In *Guide Geologiche Regionali—Guida alla Geologia del Sudalpino Centro-Orientale*; Castellarin, A., Vai, G.B., Eds.; Pitagora: Bologna, Italy, 1983; pp. 273–278. ISBN 9788837118952.
33. Blendinger, W.; Blendinger, E. Windward-leeward effects on Triassic carbonate bank margin facies of the Dolomites, northern Italy. *Sediment. Geol.* **1989**, *64*, 143–166. [CrossRef]
34. Keim, L.; Brandner, R. Facies interfingering and synsedimentary tectonics on late ladinian-early carnian carbonate platforms (Dolomites, Italy). *Int. J. Earth Sci.* **2001**, *90*, 813–830. [CrossRef]
35. De Zanche, V.; Gianolla, P.; Mietto, P.; Sjorpaes, C.; Vail, P.R. Triassic Sequence Stratigraphy in the Dolomites (Italy). *Mem. Sci. Geol.* **1993**, *45*, 1–27.
36. Stefani, M.; Brak, P.; Gianolla, P.; Keim, L.; Mauer, M.; Neri, C.; Preto, N.; Riva, A.; Roghi, G.; Russo, F. Field Guide Book P44—Triassic carbonate platforms of the Dolomites: Carbonate production, relative sealevel fluctuations and the shaping of the depositional architecture. In Proceedings of the 32nd International Geologic Congress, Florence, Italy, 20–28 August 2004; Guerrieri, L., Rischia, I., Serva, L., Eds.; APAT: Roma, Italy, 2004; Volume 5. Available online: https://www.isprambiente.gov.it/contentfiles/00006600/6621-p44.pdf (accessed on 10 January 2022).
37. Simms, M.J.; Ruffell, A.H. Synchroneity of climatic change and extinctions in the Late Triassic. *Geology* **1989**, *17*, 265–268. [CrossRef]
38. Simms, M.J.; Ruffell, A.H. Climatic and biotic change in the late Triassic. *J.-Geol. Soc.* **1990**, *147*, 321–327. [CrossRef]
39. Gattolin, G.; Breda, A.; Preto, N. Demise of late Triassic carbonate platforms triggered the onset of a tide-dominated depositional system in the dolomites, northern Italy. *Sediment. Geol.* **2013**, *297*, 38–49. [CrossRef]

40. Gattolin, G.; Preto, N.; Breda, A.; Franceschi, M.; Isotton, M.; Gianolla, P. Sequence stratigraphy after the demise of a high-relief carbonate platform (Carnian of the Dolomites): Sea-level and climate disentangled. *Palaeogeogr. Palaeoclimatol. Palaeoecol.* **2015**, *423*, 1–17. [CrossRef]
41. Roghi, G. Palynological investigations in the Carnian of the Cave del Predil area (Julian Alps, NE Italy). *Rev. Palaeobot. Palynol.* **2004**, *132*, 1–35. [CrossRef]
42. Preto, N.; Kustatscher, E.; Wignall, P.B. Triassic climates—State of the art and perspectives. *Palaeogeogr. Palaeoclimatol. Palaeoecol.* **2010**, *290*, 1–10. [CrossRef]
43. Dal Corso, J.; Mietto, P.; Newton, R.J.; Pancost, R.D.; Preto, N.; Roghi, G.; Wignall, P.B. Discovery of a major negative δ13C spike in the Carnian (Late Triassic) linked to the eruption of Wrangellia flood basalts. *Geology* **2012**, *40*, 79–82. [CrossRef]
44. Dal Corso, J.; Bernardi, M.; Sun, Y.; Song, H.; Seyfullah, L.J.; Preto, N.; Gianolla, P.; Ruffel, A.; Kustatscher, E.; Roghi, G.; et al. Extinction and dawn of the modern world in the Carnian (Late Triassic). *Sci. Adv.* **2020**, *6*, eaba0099. [CrossRef] [PubMed]
45. Bosellini, A.; Gianolla, P.; Stefani, M. Geology of the Dolomites. *Episodes* **2003**, *26*, 181–185. [CrossRef]
46. Doglioni, C. Tectonics of the Dolomites. *Bull. Fuer Angew. Geol.* **2007**, *12*, 11–15.
47. Castellarin, A.; Lucchini, F.; Rossi, P.L.; Selli, L.; Simboli, G. The Middle Triassic magmatic-tectonic arc development in the Southern Alps. *Tectonophysics* **1988**, *146*, 79–89. [CrossRef]
48. Abbas, H.; Michail, M.; Cifelli, F.; Mattei, M.; Gianolla, P.; Lustrino, M.; Carminati, E. Emplacement modes of the Ladinian plutonic rocks of the Dolomites: Insights from anisotropy of magnetic susceptibility. *J. Struct. Geol.* **2018**, *113*, 42–61. [CrossRef]
49. Bertotti, G. Subsidence, deformation, thermal and mechanical evolution of the mesozoic South Alpine rifted margin: An analogue for Atlantic-type-margins. *Geol. Soc. Spec. Publ.* **2001**, *187*, 125–141. [CrossRef]
50. Berra, F.; Carminati, E. Subsidence history from a backstripping analysis of the Permo-Mesozoic succession of the Central Southern Alps (Northern Italy). *Basin Res.* **2010**, *22*, 952–975. [CrossRef]
51. Polino, R.; Dal Piaz, G.V.; Gosso, G. Tectonic erosion at the Adria margin and accretionary processes for the Cretaceous orogeny of the Alps. *Mémoires Société Géologique Fr.* **1996**, *156*, 345–367.
52. Schmid, S.M.; Pfiffner, O.A.; Froitzheim, N.; Schönborn, G.; Kissling, E. Geophysical-geological transect and tectonic evolution of the Swiss-Italian Alps. *Tectonics* **1990**, *15*, 1036–1064. [CrossRef]
53. Caputo, R. The polyphase tectonics of Eastern Dolomites, Italy. *Mem. Sci. Geol.* **1996**, *48*, 93–106.
54. Caputo, R.; Stefani, M.M.; Dal Piaz, G. Contractional and transcurrent tectonics in the Marmolada group (Dolomites, Italy). *Mem. Sci. Geol.* **1999**, *51*, 63–77.
55. Caputo, R.; Poli, M.E.; Zanferrari, A. Neogene-Quaternary tectonic stratigraphy of the eastern Southern Alps, NE Italy. *J. Struct. Geol.* **2010**, *32*, 1009–1027. [CrossRef]
56. Schönborn, G. Balancing cross sections with kinematic constraints: The Dolomites (northern Italy). *Tectonics* **1999**, *18*, 527–545. [CrossRef]
57. Antonellini, M.; Mollema, P.N. A natural analog for a fractured and faulted reservoir in dolomite: Triassic Sella Group, northern Italy. *Am. Assoc. Pet. Geol. Bull.* **2010**, *84*, 314–344. [CrossRef]
58. Castellarin, A.; Cantelli, L.; Fesce, A.M.; Mercier, J.L.; Picotti, V.; Pini, G.A.; Prosser, G.; Selli, L. Alpine compressional tectonics in the southern Alps: Relationships with the N-Apennines. *Ann. Tecton.* **1992**, *6*, 62–94.
59. Mazzoli, S.; Helman, M. Neogene patterns of relative plate motion for Africa-Europe: Some implications for recent central Mediterranean tectonics. *Geol. Rundsch.* **1994**, *83*, 464–468. [CrossRef]
60. Menegoni, N.; Giordan, D.; Perotti, C.; Tannant, D.D. Detection and geometric characterization of rock mass discontinuities using a 3D high-resolution digital outcrop model generated from RPAS imagery—Ormea rock slope, Italy. *Eng. Geol.* **2019**, *252*, 145–163. [CrossRef]
61. QGIS.org. *QGIS Geographic Information System*; QGIS Association: Online, 2022. Available online: http://www.qgis.org (accessed on 10 January 2022).
62. Nyberg, B.; Nixon, C.W.; Sanderson, D.J. NetworkGT: A GIS tool for geometric and topological analysis of two-dimensional fracture networks. *Geosphere* **2018**, *14*, 1618–1634. [CrossRef]
63. Menegoni, N.; Meisina, C.; Perotti, C.; Crozi, M. Analysis by UAV digital photogrammetry of folds and related fractures in the Monte Antola Flysch Formation (Ponte Organasco, Italy). *Geosciences* **2018**, *8*, 299. [CrossRef]
64. CloudCompare—Open Source Project. Available online: https://www.danielgm.net/cc/ (accessed on 1 August 2022).
65. Panara, Y.; Khanna, P.; Chandra, V.; Finkbeiner, T.; Vahrenkamp, V. 3D Digital Outcrop Model-based fracture network analsysis of Reservoir Outcrop Analogue, Upper Jubaila Formation, Saudi Arabia. In Proceedings of the 3rd EAGE Annual Conference and Exibithion, Madrid, Spain, 6–9 June 2022; Volume 1, pp. 1–5. [CrossRef]
66. Thiele, S.T.; Grose, L.; Samsu, A.; Micklethwaite, S.; Vollgger, S.A.; Cruden, A.R. Rapid, semi-automatic fracture and contact mapping for point clouds, images and geophysical data. *Solid Earth* **2017**, *8*, 1241–1253. [CrossRef]
67. Tziavou, O.; Pytharouli, S.; Souter, J. Unmanned Aerial Vehicle (UAV) based mapping in engineering geological surveys: Considerations for optimum results. *Eng. Geol.* **2018**, *232*, 12–21. [CrossRef]
68. Watkins, H.; Bond, C.E.; Healy, D.; Butler, R.W. Appraisal of fracture sampling methods and a new workflow to characterise heterogeneous fracture networks at outcrop. *J. Struct. Geol.* **2015**, *72*, 67–82. [CrossRef]
69. Menegoni, N.; Giordan, D.; Inama, I.; Perotti, C. DICE: An open-source MATLAB application for quantification and parametrization of Digital Outcrop Model-based fracture datasets. *J. Rock Mech. Geotech. Eng.* 2022, in press. [CrossRef]

70. DICE—GitHub Repository. Available online: https://github.com/nicmenegoni/DICE (accessed on 1 August 2022).
71. Sanderson, D.J.; Nixon, C.W. The use of topology in fracture network characterization. *J. Struct. Geol.* **2015**, *72*, 55–66. [CrossRef]
72. Koša, E.; Hunt, D.W. Growth of syndepositional faults in carbonate strata: Upper Permian Capitan platform, New Mexico, USA. *J. Struct. Geol.* **2005**, *27*, 1069–1094. [CrossRef]
73. Frost, E.L.; Kerans, C. Platform-margin trajectory as a control on syndepositional fracture patterns, Canning Basin, Western Australia. *J. Sediment. Res.* **2009**, *79*, 44–55. [CrossRef]
74. Sharp, I.; Gillespie, P.; Morsalnezhad, D.; Taberner, C.; Karpuz, R.; Vergés, J.; Horbury, A.; Pickard, N.; Garland, J.; Hunt, D. Stratigraphic architecture and fracture-controlled dolomitization of the Cretaceous Khami and Bangestan groups: An outcrop case study, Zagros Mountains, Iran. *Geol. Soc. Spec. Publ.* **2010**, *329*, 343–396. [CrossRef]
75. Berra, F.; Carminati, E. Differential compaction and early rock fracturing in high-relief carbonate platforms: Numerical modelling of a Triassic case study (Esino Limestone, Central Southern Alps, Italy). *Basin Res.* **2012**, *24*, 598–614. [CrossRef]
76. Budd, D.A.; Frost, E.L.; Huntington, K.W.; Allwardt, P.F. Syndepositional Deformation Features in High-Relief Carbonate Platforms: Long-Lived Conduits for Diagenetic Fluids. *J. Sediment. Res.* **2013**, *83*, 12–36. [CrossRef]
77. La Bruna, V.; Agosta, F.; Prosser, G. New insights on the structural setting of the Monte Alpi area, Basilicata, Italy. *Ital. J. Geosci.* **2017**, *136*, 220–237. [CrossRef]
78. La Bruna, V.; Agosta, F.; Lamarche, J.; Viseur, S.; Prosser, G. Fault growth mechanisms and scaling properties in foreland basin system: The case study of Monte Alpi, Southern Apennines, Italy. *J. Struct. Geol.* **2018**, *116*, 94–113. [CrossRef]
79. Mollema, P.N.; Antonellini, M. Development of strike-slip faults in the dolomites of the Sella Group, Northern Italy. *J. Struct. Geol.* **1999**, *21*, 273–292. [CrossRef]